Computers and Geotechnics 176 (2024) 106751

Contents lists available at ScienceDirect

Computers and Geotechnics

journal homepage: www.elsevier.com/locate/compgeo

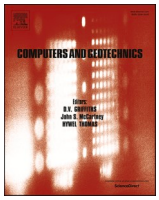

Numerical framework for coupling SPH with image-based DEM for irregular particles

Mehryar Amir Hosseini , Pejman Tahmasebi *

Colorado School of Mines, Golden, CO 80401, USA

ARTICLE INFO

Keywords:
Fluid-particle interaction
SPH
Irregular particles
Coupling
Image-based DEM

ABSTRACT

Understanding fluid-particle interactions is crucial due to their occurrence in both natural phenomena and engineering applications, but accurately capturing these interactions presents considerable challenges. The complexity escalates when accounting for the natural shape of particles, prompting the development of numerical solutions to address these complexities. Here, we propose a numerical framework that combines Smoothed Particle Hydrodynamics (SPH) with the Imaged-based Discrete Element Method (iDEM) to model the fluid and particle components, respectively, while considering the actual shape of particles. Initially, we validated our approach by simulating sphere and cube water entry cases, confirming the method's accuracy. Later, we applied the coupling scheme to a more complex scenario of a dam break, involving irregular and cubic grains of equivalent mass and volume. Our results demonstrate the effectiveness of the proposed scheme in capturing the actual shape of grains and elucidate the influence of particle shape on various fluid parameters. We found that fluid movement is facilitated more in cubic packs due to reduced interlocking and increased surface area, resulting in higher fluid and particle velocities and enhanced displacement in cube-shaped grains. These findings deepen our understanding of fluid-particle interactions in complex systems and the significance of particle shape in such analyses.

1. Introduction

Fluid-particle interactions can be seen in a wide range of engineering problems, such as landslides (Amir Hosseini and Tahmasebi, 2023; Ataie-Ashtiani and Shobeyri, 2008), dam breaks (Ancey et al., 2013; Lai et al., 2023; Shakibaeinia and Jin, 2011), Debris flow (Kong et al., 2022; Meng and Wang, 2016; Pastor et al., 2023; Wang et al., 2016), sandpiles (Zhang and Tahmasebi, 2022a), etc. Understanding these interactions is essential for analyzing and potentially predicting such phenomena. In these problems, the presence of the fluid phase adds complexity to the system, as the fluid can alter the arrangement and motion of particles. For instance, in scenarios like dam breaks, the fluid alone can induce particle movement, leading to system instability. Predicting such systems with precision is challenging due to the intricate nature of fluid-particle interactions. Moreover, in real-world scenarios, particles often exhibit irregular shapes, further complicating the analysis. While experimental investigations offer insights into fluid-particle interactions, monitoring these interactions can be costly and prone to inaccuracies due to equipment limitations and not being able to observe every single phenomenon. Hence, numerical methods serve as a valuable alternative for capturing these interactions with the desired level of accuracy. A comprehensive review on the available experimental and computational methods along with the recent developments across different fields and applications can be found elsewhere (Tahmasebi, 2023).

As previously mentioned, numerical methods must effectively address three distinct aspects of a fluid-particle system: (*i*) particle–particle interactions, (*ii*) fluid-particle interactions, and (*iii*) fluid movement. To address the first aspect, the Discrete Element Method (DEM) has emerged as a powerful tool for modeling particle–particle interactions in various applications (Cundall and Strack, 1979). Traditionally, DEM calculates the trajectory of individual particles in the domain based on Newton's second law of motion, treating each particle as a discrete entity. However, conventional DEM approaches typically represent particles as spheres, overlooking their actual shapes (Tahmasebi, 2018). To overcome this limitation, several techniques have been developed to incorporate the natural shapes of particles (Kawamoto et al., 2018, 2016; Zhao et al., 2023). Among these methods,

* Corresponding author.
E-mail address: tahmasebi@mines.edu (P. Tahmasebi).

https://doi.org/10.1016/j.compgeo.2024.106751

Available online 13 September 2024

the multi-sphere approach is widely used (Angelidakis et al., 2021; Farivar et al., 2020; Li et al., 2015; Liu et al., 2021; Zhou et al., 2017), where a cluster of overlapped spheres is employed to approximate the particle's shape. Despite its popularity, this method has drawbacks, including increased computational costs due to the need for numerous overlapping spheres to mimic complex particle shapes. Moreover, it struggles to accurately represent particles with complex convex or concave features. Alternative methods such as polyhedral and ellipsoid techniques offer improvements in capturing particle morphology, although they still fall short of accurately reproducing real grain shapes (Azéma et al., 2013; Höhner et al., 2011; Liu et al., 2021). Additionally, approaches considering rolling friction effects can be utilized to incorporate particle morphology, albeit requiring calibration with experimental data (Wensrich and Katterfeld, 2012). Furthermore, we believe that the shape of particles cannot be replaced with unrealistic inter-granular friction, but the actual morphology of particles should be used directly.

Therefore, a more advanced technique is required to accurately represent the morphology of grains and compute inter-particle forces. The Image-based Discrete Element Method (iDEM) has demonstrated its effectiveness in achieving these objectives (Amir Hosseini and Tahmasebi, 2023; Hosseini and Tahmasebi, 2024; Zhang and Tahmasebi, 2023, 2022b, 2022a). Initially, XRCT (X-ray computed tomography) images are processed using image analysis methods within this approach. iDEM then defines a function in the coordinate system (α), dividing the domain into three distinct zones: (*i*) points or pixels inside a grain ($\alpha > 0$), (*ii*) points or pixels on the particle surface ($\alpha = 0$), and (*iii*) points or pixels outside the particle ($\alpha < 0$) (Houlsby, 2009). Various studies have been conducted to enhance the accuracy of these functions, with the iDEM incorporating Enhanced Distance Transform (EDT) being a notable example. Previous research (Zhang and Tahmasebi, 2022b) has demonstrated that EDT improves both accuracy and computational efficiency. Leveraging these capabilities, we employed the iDEM methodology to accurately capture grain morphology and perform inter-particle and particle–wall calculations.

Once the iDEM is utilized for particle–particle interactions while the shape of particle is taken into account, an accurate method is required to model fluid movements. Two main approaches are commonly used for this purpose: the Lagrangian and Eulerian methods. The Lagrangian approach is particle-based, while the Eulerian approach is grid-based. The Eulerian method, a traditional Computational Fluid Dynamics (CFD) approach, has demonstrated its efficacy in various applications (Amir Hosseini et al., 2023; Amir Hosseini and Tahmasebi, 2024; Knight et al., 2020; Pozzetti and Peters, 2018; Zhang and Tahmasebi, 2019). However, it has limitations, particularly in capturing fluid-particle interactions. For instance, the resolved CFD-DEM requires a fine-meshed domain to accurately define the boundaries of particles, resulting in increased computational costs (Amir Hosseini et al., 2023; Zhang and Tahmasebi, 2022a, 2018; Tahmasebi and Kamrava, 2019), while unresolved CFD methods cannot represent the shape of particles.

Alternatively, meshless techniques, which are particle-based, offer a solution to the complexity of meshing (Sun et al., 2023). These techniques not only simplify mesh complexity but also effectively handle complex hydrodynamic problems. Such methods fall under the category of Lagrangian methods, ensuring faster coupling. Meshless techniques have gained significant attention due to several advantages. Unlike grid-based CFD methods, where fluid is considered a continuum phase, meshless methods discretize the fluid using particles. Smoothed Particle Hydrodynamics (SPH) (Bui and Nguyen, 2021; Lian et al., 2021; Ma et al., 2022; Xu and Dong, 2021), Finite Pointset Method (FPM) (Saucedo-Zendejo and Reséndiz-Flores, 2023), Radial Basis Function (RBF) (Xiao et al., 2023), and Moving Particle Semi-implicit (MPS) (Xu et al., 2023) are some of the meshless methods developed. Among these, SPH has been widely employed in various studies due to its efficiency and accuracy. Furthermore, both SPH and iDEM are Lagrangian techniques, facilitating more efficient and faster fluid-particle interaction calculations. Therefore, in this paper, we utilize the SPH method to model fluid movement (Domínguez et al., 2021).

Up to this point, we have outlined our methodologies for computing particle–particle interactions and fluid movements. In addressing the fluid-particle interactions between SPH and DEM, the SPH-DEM method has found applications across various domains, including dam break scenarios (Liu et al., 2022), landslide-generated waves (Bu et al., 2022), debris flow (Canelas et al., 2017), and sediment transport (Tran-Duc et al., 2017). While some techniques can accommodate irregular grain shapes, such as the polyhedral method within the DEM component of the coupling, capturing the realistic shape of particle in DEM approaches remain somewhat limited, and the integration of such methods with SPH has been noticeably absent from the literature. To be more specific, the two-way coupling between Weakly Compressible SPH (WCSPH) and Distributed Contact DEM (DCDEM) has been proposed in previous investigation, where applied on the debris flow with the cubic and cylinder grains (Canelas et al., 2016). Other numerical investigation also applied the WCSPH-DEM with spherical particles (He et al., 2018). Penalty approach also has been deployed in numerical investigation to couple the Incompressible SPH (ISPH) with DEM with utilizing the energy tracking impulse (Asai et al., 2021). In other study (Wu et al., 2016), the SPH has been coupled with the conventional DEM in 2D to model flexible plates with clump of DEM particles. The elastic beam is also studied with deploying the SPH-DEM technique (Capasso et al., 2022). As discussed, therefore, there is a clear research gap in consideration of the real shape of particles in SPH-DEM coupling approaches.

To bridge this research gap, we propose a coupling approach that links iDEM with SPH. Here, iDEM is tasked with handling particle–particle interactions, SPH computes fluid movements, and the coupling mechanism facilitates the transfer of forces between the fluid and particles bidirectionally. Once the coupling between SPH and iDEM has been established, it becomes crucial to validate its accuracy through experimental studies. To achieve this, we will conduct validation tests using two scenarios: a sphere water entry based on experimental investigations (Aristoff and Bush, 2009) and a semi-submerged cube water entry (Wu et al., 2014). By comparing our computational results with the experimental data, we can verify the fidelity of our proposed coupling. Following successful validation, we will apply the validated coupling model to simulate a dam break scenario, considering irregular and cubic particles. This application will demonstrate the effectiveness and reliability of our coupling approach in capturing real-world phenomena.

The remaining sections of this paper are structured as follows. Section 2 discusses the governing equations of iDEM, SPH, and their coupling. In Section 3, we present, discuss, and compare the results of validation tests against experimental studies. Section 4 details the implementation of our developed code in dam break scenarios involving irregular and cubic particles, along with the corresponding results and discussions. Finally, Section 5 provides a summary of the paper and outlines its conclusions.

2. Numerical Method

This section explains the proposed coupling method to model a fluid-particle system. As elaborated, the coupling consists of three segments to simulate such a complex approach. The first is the iDEM, responsible for particle–particle and particle–wall interactions. The SPH part calculates the fluid movement and the coupling procedure, which connects the SPH with iDEM. Hence, the iDEM, the SPH, and coupling will be detailed in this section.

2.1. Image-based Discrete Element Method (iDEM)

2.1.1. Image Analysis

The 3D binary image set, obtained through XRCT, provides a faithful representation of particle shapes, requiring interpretation for

computational purposes. Image analysis techniques, such as the EDT, offer a reliable means to achieve this. Initially, the binary image is divided into object and background zones, after which the EDT computes the shortest distances between background and object pixels using the Euclidean distance method (Zhang and Tahmasebi, 2022a). This process assigns specific distance values to each pixel, where pixels inside the particle (object zone) yield positive values, while those outside register negative values. Here, Gaussian filtration and trilinear interpolation are applied to the EDT results, smoothing out sharp transitions and accurately delineating particle surfaces. Thus, the particle's natural shape is realistically captured and can be seamlessly integrated into computational codes. Similar to traditional discrete element methods, iDEM needs information about particle properties such as center of mass, moment of inertia, mass, and volume. The EDT 3D field enables the calculation of these properties, ensuring accurate representation of particles within the computational framework. Further details on EDT and property calculations are available elsewhere (Amir Hosseini and Tahmasebi, 2023; Hosseini and Tahmasebi, 2024; Zhang and Tahmasebi, 2023, 2022b). Fig. 1 illustrates the EDT in iDEM.

2.1.2. Particle Interaction

In this section, we will discuss the process we employed to compute particle interactions, particularly focusing on contact detection. Contact detection in standard DEM is straightforward as it deals with spherical particles. Typically, in conventional DEM, contact between spherical particles is identified by comparing the centers of the spheres. The contact is then established, allowing for the calculation of particle–particle or particle–wall force values based on the overlap. However, contact detection and calculation become challenging for irregular particles due to two main reasons: (*i*) determining when particles are in contact, and (*ii*) calculating the overlap necessary for force calculation. To address these complexities, we implemented the node-to-surface method in iDEM. This technique involves systematically placing nodes on the surface of particles. Our previous studies have extensively discussed the node-to-surface approach (Amir Hosseini and Tahmasebi, 2023; Hosseini and Tahmasebi, 2024; Zhang and Tahmasebi, 2022b, 2022a).

To identify particles in contact, the center of mass of each particle (particle i) is compared with others within the domain. Instead of examining every particle in the domain, iDEM identifies potential in-contact particles and subsequently checks for overlap. This process entails defining a detection radius (R_g), which should be several times larger than the average radius of the grains to prevent overlooking contact between particles. Once the detection radius is established, the center of mass of particle i is compared with other particles. If a particle lies within the detection radius, it is considered a potential in-contact particle with particle i. Therefore, particles in the domain are classified as either potentially in-contact or non-contact particles. This approach significantly reduces the computational cost of iDEM.

Once nodes are positioned on the grains and potential in-contact particles are identified, iDEM proceeds to examine overlaps for the parent grain, denoted as grain i. In this process, the nodes on potential in-contact particles are compared to the distance field of grain i. Specifically, if the coordinate of a node on particle j (C_{n_j}) yields a positive value in grain i's distance field ($D^i_{C_{n_j}} > 0$), particle i and particle j are considered as in-contact particles. This comparison is performed for all potential in-contact particles. Then, the inter-particle force can be determined based on the overlap (δ) between the in-contact particles.

2.1.3. Particle movement

After calculating the overlap between two irregular particles, the motion of each particle should be calculated. To this end, the general concepts of the DEM can be deployed. In DEM, each particle can go through rotational and/or transitional movement, which follows Newton's second law of motion and Euler's equations. Hence, the transitional and angular motion of each particle can be expressed as follows:

$$m_i\frac{d\boldsymbol{V}_i}{dt} = \sum_j \boldsymbol{F}_{ij}^{p-p} + \sum_w \boldsymbol{F}_{iw}^{p-w} + \boldsymbol{F}_i^{f-p} + \boldsymbol{F}_i^{g}, \tag{1}$$

$$I_i\frac{d\boldsymbol{\omega}_i}{dt} + \boldsymbol{\omega}_i \times (I_i\boldsymbol{\omega}_i) = \sum_j \boldsymbol{T}_{ij}^{p-p} + \sum_w \boldsymbol{T}_{w}^{p-w} + \boldsymbol{T}_i^{p-f}, \tag{2}$$

where m_i, $\boldsymbol{V}_i$, I_i, and $\boldsymbol{\omega}_i$ are the mass, velocity, inertia, and rotational velocity of particle i, respectively. Moreover, $\sum_j \boldsymbol{F}_{ij}^{p-p}$ is the summation of particle–particle force between particle i and in-contact grains (j). $\sum_w \boldsymbol{F}_{iw}^{p-w}$ is the sum of particle–wall forces, and $\boldsymbol{F}_i^{f-p}$ is fluid-particle interaction force. $\boldsymbol{F}_i^{g}$ is the gravitational force applied on particle i. Furthermore, in Eq. (2), $\sum_j \boldsymbol{T}_{ij}^{p-p}$ and $\sum_w \boldsymbol{T}_{w}^{p-w}$ are the torque acting on particle i causing by in-contact particles and particle–wall interactions, respectively. The fluid can also apply torque on particle i, defined as $\boldsymbol{T}_i^{p-f}$. The inter-particle force ($\sum_j \boldsymbol{F}_{ij}^{p-p}$) expands as follows:

$$\sum_j \boldsymbol{F}_{ij}^{p-p} = \sum_{n=1}^{N} \boldsymbol{F}_{ij}^{n} + \sum_{n=1}^{N} \boldsymbol{F}_{ij}^{t}, \tag{3}$$

such that,

$$\boldsymbol{F}_{ij}^{n} = -k_n\delta\vec{\boldsymbol{n}}_{ij}, \tag{4}$$

$$\boldsymbol{F}_{ij}^{t} = R\left(\boldsymbol{F}_{ij}^{t}\right)_{T+\Delta t} - k_t\left[\boldsymbol{V}_{ij} - \left(\boldsymbol{V}_{ij}.\vec{\boldsymbol{n}}_{ij}\right)\vec{\boldsymbol{n}}_{ij}\right]\Delta t, \tag{5}$$

where, N is the number of overlapped nodes on the surface of particle i. $\boldsymbol{F}_{ij}^{n}$ and $\boldsymbol{F}_{ij}^{t}$ are the normal and tangential forces, respectively. k is the normal stiffness, R is the rotational matrix, T is the previous time step, and Δt is the time increment (i.e., time step). k_n and k_t are normal and

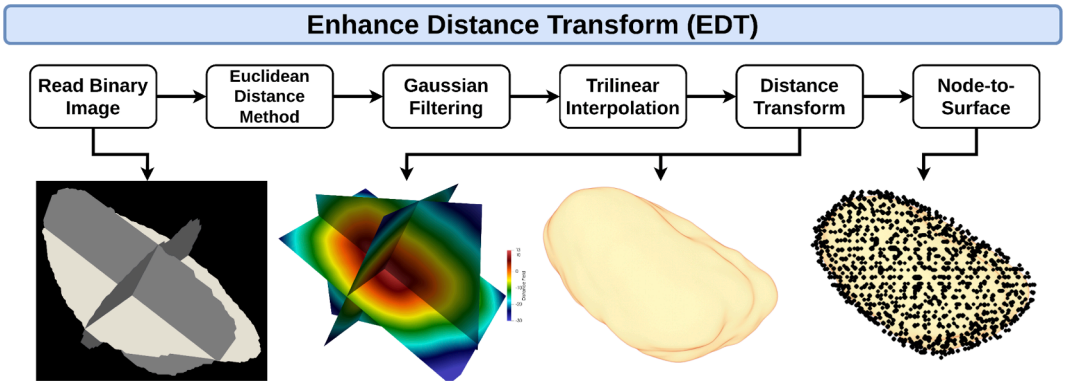

Fig. 1. The Enhanced Distance Transform (EDT) implemented in the iDEM.

tangential stiffness, and $\vec{n}_{ij}$ is the contact normal vector. $\boldsymbol{V}_{ij}$ presents relative velocity, which can be calculated using:

$$\boldsymbol{V}_{ij} = \boldsymbol{V}_i + \boldsymbol{\omega}_i \times \left(\vec{C}_c - \vec{c}^{\,i}_m\right) - \boldsymbol{V}_j - \boldsymbol{\omega}_j \times \left(\vec{C}_c - \vec{c}^{\,j}_m\right), \tag{6}$$

where $\vec{C}_c$ is the position of the overlapped node. $\vec{c}^{\,i}_m$ and $\vec{c}^{\,j}_m$ are the center of mass of particle i and j. Moreover, the Coulomb friction law has been implemented to calculate $\boldsymbol{F}^t_{ij}$ as follows:

$$\boldsymbol{F}^t_{ij} = \frac{\boldsymbol{F}^t_{ij}}{\|\boldsymbol{F}^t_{ij}\|} \min(\|\boldsymbol{F}^t_{ij}\|, \mu \boldsymbol{F}^n_{ij}) \tag{7}$$

where μ is friction coefficient. Then, the action-reaction rule is applied where $\boldsymbol{F}_{ij} = -\boldsymbol{F}_{ji}$.

2.1.4. Image-Based DEM Algorithm

To sum up, the iDEM follows the mentioned steps to calculate particle–particle interactions which are summarized in Algorithm 1.

Algorithm 1: Implemented image-based dem algorithm

```
Input: 3D binary matrix for number of particles
Output: inter-particle force and torque
for i = 0, nParticle do
    Read Binary images
    Apply the Euclidean Distance Method, Gaussian Filtering, and Trilinear interpolation
    Calculating Distance Field
    Apply node-to-surface technique
end for
for i = 0, nParticle do
    Finding potential in-contact particles
    Check overlap between potential in-contact particles
        if overlap == True
            Calculate overlap and normal vector
            Calculate Transitional and rotational motion ← Eqs. (1)-(7)
            Apply calculated force and torque to the particles
        end if
end for
```

2.2. Smoothed Particle Hydrodynamic (SPH)

In this section, we discuss the fundamental principles of the SPH method (Domínguez et al., 2021). To provide a comprehensive understanding of the SPH method, we will begin by explaining the governing equations pertaining to fluid–fluid particle interactions and fluid-body interactions.

2.2.1. Governing Equations

As previously mentioned, SPH is a Lagrangian method that discretizes a continuous phase into particles. Therefore, in line with Lagrangian principles, this meshless technique computes the motion of each particle. Given that the properties of a target particle are influenced by its neighboring particles, a weighting function is employed to account for this influence. This is typically achieved through the application of a kernel function, which can be represented for a function $f_{(p)}$ as follows:

$$f_{(p)} = \int f_{(p')} K(p - p', s) dp', \tag{8}$$

where $\boldsymbol{p}$ and $\boldsymbol{p}'$ are defined as the target particle's position and the particle's temporary position. Also, $\boldsymbol{s}$ is smoothing length, and K is the weighting function. The above equations in discrete computational can be presented as:

$$f_{(p)} = \sum_n f_{(p'_n)} K(p'_n - p_n, s) \frac{m_n}{\rho_n}, \tag{9}$$

where n is the neighboring particle, m_n and ρ_n are the mass and density of neighboring particles, respectively. The Quintic Wendland Kernel (Wendland, 1995) is applied in Eq. (9), which is a specific kernel function used to interpolate properties between particles. It belongs to the family of Wendland functions, which are commonly employed in SPH due to their smoothness and compact support. The Quintic Wendland Kernel has a quintic polynomial form and is characterized by its ability to accurately represent gradients and smooth out discontinuities in the fluid properties. It effectively mitigates numerical noise and instability issues often encountered in SPH simulations, making it an accepted choice for modeling various fluid dynamics phenomena with high fidelity. The kernel function's compact support ensures that only nearby particles significantly influence the interpolation, contributing to computational efficiency and reducing the computational cost of SPH simulations.

To calculate fluid motions in a discrete domain, one way is writing the Navier-Stokes equation in discrete form. Then, the discrete Navier-Stokes equation can solve fluid particles' motion; therefore, the momentum equation can be written as:

$$\frac{d\boldsymbol{v}_p}{dt} = -\sum_n m_n \left(\frac{\boldsymbol{p}_n + \boldsymbol{p}_p}{\rho_n \rho_p}\right) \nabla_p K_{p-n} + \boldsymbol{g} + \Phi_p, \tag{10}$$

where $\boldsymbol{v}_p$ is the velocity of the target point, K_{p-n} is kernel function for particle p, $\boldsymbol{g}$ is gravitational acceleration, $\boldsymbol{p}$ is the pressure, and Φ_p is the artificial viscosity term, which can be written in the following form for the artificial viscosity (Domínguez et al., 2021):

$$\Phi_p = -\sum_n m_n \Psi_{np} \nabla_p K_{p-n}, \tag{11}$$

in which:

$$\Psi_{np} = \begin{cases} \left(\frac{-\alpha C_{s-np}}{\rho_{np}}\right)\left(\frac{s \boldsymbol{v}_{np} \cdot \boldsymbol{p}_{np}}{{p_{np}}^2 + 0.01 s^2}\right) & \boldsymbol{v}_{np} \cdot \boldsymbol{p}_{np} < 0 \\ 0 & \boldsymbol{v}_{np} \cdot \boldsymbol{p}_{np} > 0 \end{cases} \tag{12}$$

where α is the artificial viscosity coefficient, and C_{S-np} and ρ_{np} is the mean of the speed of sound density of the target particle (i.e., p) and neighboring's (i.e., n), respectively.

In the implemented SPH simulation, a weakly compressible SPH concept is used in the governing equations (Domínguez et al., 2021). Hence, fluid pressure can be calculated as:

$$P = \frac{{C_S}^2 \rho_f}{\eta} \left[\left(\frac{\rho}{\rho_f}\right)^{\eta} - 1\right], \tag{13}$$

where P is the fluid pressure, C_S is the speed of sound, ρ_f is the reference density of the fluid, and η is polytropic constant.

Like the momentum equation (i.e., Eq. 10), continuity equitation also can be discretized as follows:

$$\frac{d\rho_p}{dt} = \sum_n m_n v_{np} \cdot \nabla_p K_{p-n} + 2\varepsilon_D s C_S \sum_n \left(\rho^{total}_{np} - \rho_f g z_{np}\right) \frac{\boldsymbol{p}_{np} \cdot \nabla_p K_{p-n}}{{\boldsymbol{p}_{np}}^2} \frac{m_n}{\rho_n}, \tag{14}$$

where the second term on the right side of Eq. 14 is the density diffusion term obtained from Fourtakas et al. (Fourtakas et al., 2019). ε_D is the diffusion coefficient, C_S is the speed of sound, ρ^{total}_{np} is the total component of density, and z_{np} is the vertical height between the target point (p) and the neighbor (n).

2.2.2. Boundary Conditions

The Dynamic Boundary Condition (DBC) and modified Dynamic Boundary Condition are boundary treatment methods used in SPH simulations, particularly in the DualSPHysics framework. DBC, initially proposed by Crespo et al. (Crespo et al., 2007), dynamically adjusts the density of boundary particles based on their proximity to fluid particles.

When fluid particles approach the boundary, the density of boundary particles increases, leading to alterations in the pressure field. Despite its widespread application and proven capability, accuracy, and efficiency in various SPH simulations, DBC exhibits certain drawbacks. In particular, density calculations at boundaries may produce unrealistic results, leading to visible gaps between fluid and boundary particles. Furthermore, pressure measurements near boundaries may exhibit noise, potentially impacting the overall accuracy of simulation results. To address these limitations, modifications to the DBC method have been proposed, aiming to improve the accuracy and realism of boundary treatments in SPH simulations.

The limitations associated with the DBC have provoked the development of modified versions, such as the modified Dynamic Boundary Condition (mDBC) (English et al., 2022). Unlike DBC, which adjusts the density of boundary particles dynamically, mDBC employs multiple layers of boundary particles to form the boundary interface. In mDBC, a mirroring procedure is implemented to create ghost nodes within the fluid region. These ghost nodes mimic the behavior of neighboring fluid particles, allowing the calculation of fluid properties at the boundary particles. It is essential to note that the normal vector at boundary particles is required for ghost node creation. Based on the mDBC, the boundary particles have zero velocity, and pressure Neumann boundary conditions are approximated at higher order, leading to improved results compared to the DBC. The formulations of the modified DBC (mDBC) are detailed elsewhere (Domínguez et al., 2021; English et al., 2022). The comparison between DBC and mDBC is visually depicted in Fig. 2, highlighting the differences in their approaches to boundary treatment in SPH simulations.

2.2.3. Fluid and Rigid-Body Interaction

In our calculations of fluid-body interaction, we aim to precisely compute these interactions. By thoroughly assessing the fluid forces acting on each boundary particle stemming from individual fluid particles, we can accurately determine the net force exerted by the fluid on a rigid body (F_{f-B}). This net force, denoted as F_{f-B}, manifests as the cumulative sum of all forces imparted by fluid particles onto each particle constituting the rigid body (p_B):

$$\left(\boldsymbol{F}_{f-B}\right)_{p_B} = \sum_{n} \left(\boldsymbol{F}_{f-B}\right)_{n}, \tag{15}$$

where n is a specific fluid particle and p_B is the rigid-body target particle. Also, $\left(F_{f-B}\right)_n$ is the force per mass from each fluid particle on each rigid body particle. $\left(\boldsymbol{F}_{f-B}\right)_{p_B}$ is calculated from Eq. (10) wherein the viscous formulation is also included in the estimation. Moreover, considering density diffusion term in Eq. (14) allows one to correct the density calculation at the interface.

After calculating the force, the rigid body's angular and linear velocity should be calculated. To this end, the aforementioned equations of the motion (i.e., Eqs. (1) and (2)) should be rewritten as follows:

$$m_B \frac{d(\boldsymbol{V}_B)_{f-p}}{dt} = \sum_{p_B} \left(\boldsymbol{F}_{f-B}\right)_{p_B}, \tag{16}$$

$$I_B \frac{d(\boldsymbol{\omega}_B)_{f-p}}{dt} + \boldsymbol{\omega}_{Bf-p} \times \left(I_B \boldsymbol{\omega}_{Bf-p}\right) = \sum_{p_B} m_{p_B} \boldsymbol{d}_{p_B}^{cm} \times \left(\boldsymbol{F}_{f-B}\right)_{p_B}, \tag{17}$$

where m_B is the mass of rigid body, $(\boldsymbol{V}_B)_{f-p}$ is the linear velocity which is exerted by the fluid on rigid-body, m_{p_B} is the mass of rigid-body node, $(\boldsymbol{\omega}_B)_{f-p}$ is the angular velocity which is applied on rigid-body from fluid, and $\boldsymbol{d}_{p_B}^{cm}$ is the distance from p_B to the center of the mass of the rigid body.

2.3. SPH-iDEM Coupling

In the proposed SPH-iDEM two-way coupling approach, the simulation initiation commences with the user, wherein the SPH module reads pertinent parameters. Next, the initialization of grains within the iDEM framework ensues. Should pre-simulation steps be necessary within the iDEM, such as particle settlement within the domain, these are executed accordingly. Following this initialization phase, essential floating (rigid body) data, such as position information, is transmitted to the SPH code for further processing. In parallel, the SPH code computes fluid particle dynamics utilizing the described formulations, thereby capturing the complex interplay between fluid and particle phases. Integral to this process is the calculation of fluid particle impacts on rigid

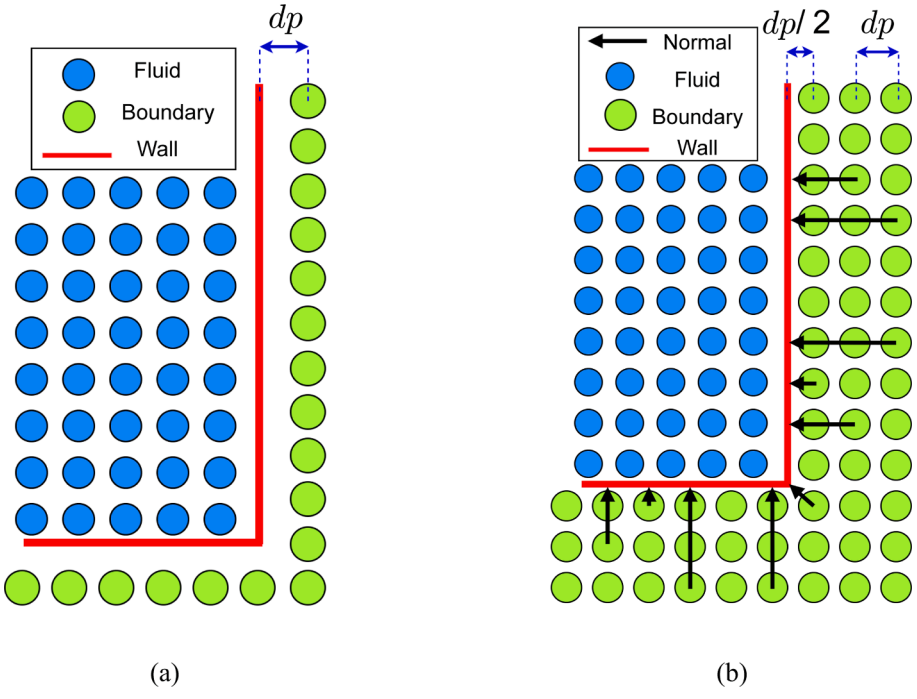

Fig. 2. Illustration of (a) the Dynamic Boundary Condition (DBC) and modified Dynamic Boundary Condition (mDBC).

bodies, which are then evaluated in terms of linear and angular velocity. The computed velocities are therefore transformed into corresponding linear (a_l) and rotational (a_w) accelerations, aiding continuous integration and accurate representation of fluid-grain interactions within the coupled framework, which are defined as:

$$a_l = \frac{d(\boldsymbol{V}_B)_{f-p}}{dt}, \tag{18}$$

$$a_w = \frac{d(\boldsymbol{\omega}_B)_{f-p}}{dt}. \tag{19}$$

The calculated accelerations are transformed into force $\left(\boldsymbol{F}_{f-B}\right)_B$ and torque $\left(\boldsymbol{T}_{f-p}\right)_B$ on rigid body:

$$\left(\boldsymbol{F}_{f-B}\right)_B = m_B \boldsymbol{a}_l, \tag{20}$$

$$\left(\boldsymbol{T}_{f-p}\right)_B = I_B \boldsymbol{a}_w. \tag{21}$$

In the proposed coupling framework, the external force and torque computed within the SPH module are transferred to the iDEM code, where they are applied as external force and torque on individual grains. Then, the grains are categorized into two distinct groups: (*i*) potential in-contact grains and (*ii*) no-contact grains. For potential in-contact grains, overlap detection is performed to determine inter-particle interactions, with successive calculations conducted accordingly. Additionally, grains are examined for overlap with the domain walls, and if any overlap is detected, the corresponding force and torque exerted by the walls are computed. Following these computations, the linear and rotational velocity as well as the position of each particle are updated within the domain. Specifically, this updated information regarding particle position and dynamics is then transmitted back to the SPH code to enable the concurrent updating of rigid-body information. Later, the fluid particles are updated based on the revised grain dynamics, ensuring consistency and accuracy in the fluid-particle coupling. This iterative process continues until the end of the simulation, ensuring comprehensive and continuous synchronization between the fluid and particle phases. Visual representations of the coupling process and the associated algorithmic workflow are provided in Fig. 3 and Fig. 4, respectively. As can be seen in Fig. 3, the density of fluid's particles in the implemented SPH is considered such that the morphology of particles are captured precisely.

3. Validations

To validate the proposed SPH-iDEM framework, it is crucial to compare its performance against experimental data. As such, two distinct experimental studies conducted in three-dimensional (3D) setups have been identified for validation purposes (Aristoff and Bush, 2009; Wu et al., 2014). The first experimental scenario involves sphere water entry with an initial velocity, which will be thoroughly examined and discussed in section 3.1 of the study. Then, the results obtained from our computational simulations will be thoroughly examined and juxtaposed against the experimental findings to assess the accuracy of our proposed framework. Furthermore, the settlement case of a semi-submerged cube will be explored, with a comprehensive analysis of the computational outcomes versus the experimental data. This comparative analysis serves as a robust validation mechanism, enabling us to find out the reliability and efficacy of the SPH-iDEM coupling approach in accurately capturing the dynamic fluid-particle interactions observed in real-world experimental scenarios.

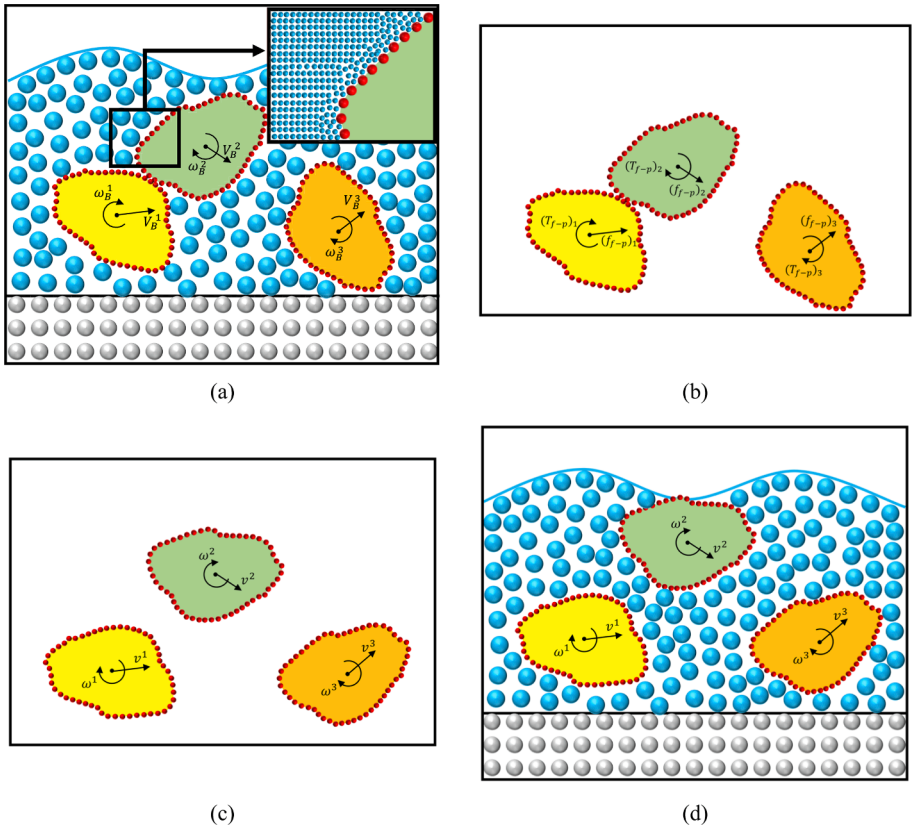

Fig. 3. Demonstration of coupling procedure in the proposed SPH-iDEM, (a) the rotational and linear velocities exerted by the fluid on grains are calculated in the SPH part. For the sake of representation, the size of SPH's particles is exaggerated but a more realistic window showing the size of SPH's particles is shown. (b) The torque and force are applied to grains in the iDEM platform. (c) inter-particle and particle–wall force and torque are calculated in the iDEM and particles motions are updated in the iDEM, (d) the updated position of grains and linear and angular velocity of them are transferred back to the SPH framework.

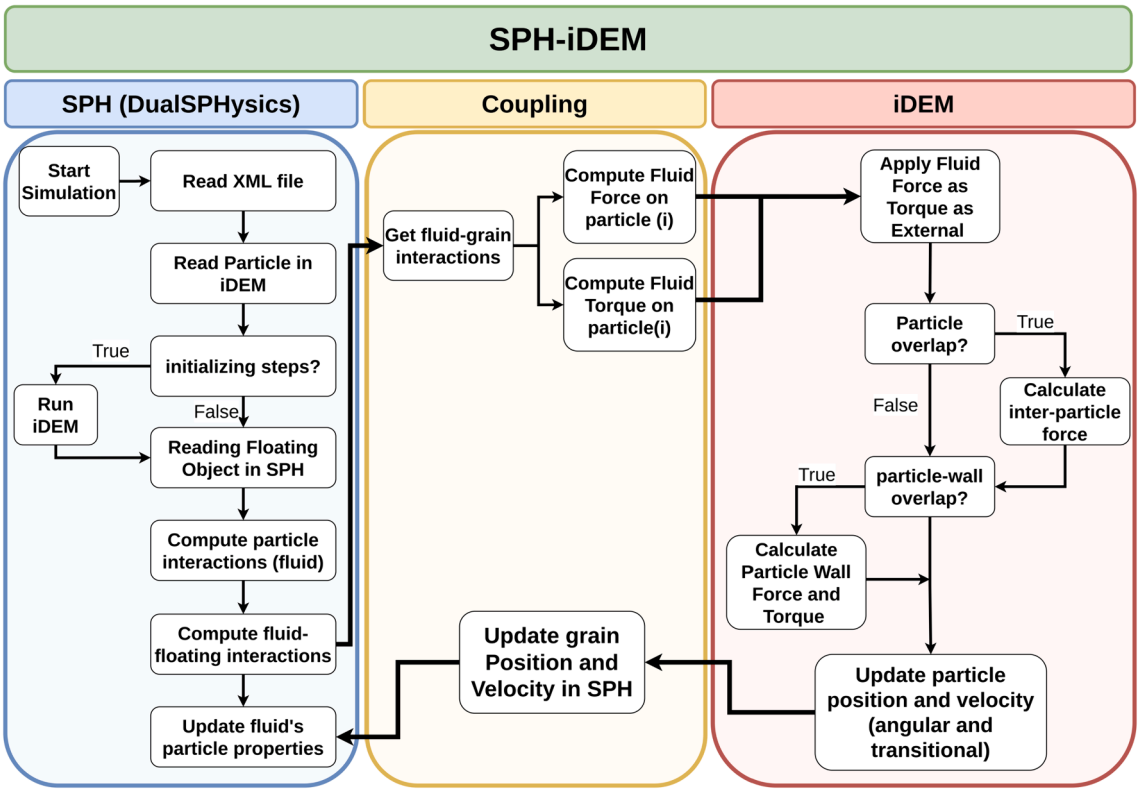

Fig. 4. The implemented SPH-iDEM coupling approach algorithm.

3.1. Single sphere water entry

For the validation of our proposed framework, we have utilized experimental data from a prior study (Aristoff and Bush, 2009). In our numerical setup, the computational domain dimensions are specified as 0.2 m × 0.2 m × 0.2 m, mirroring the dimensions employed in the experimental study. The water depth within the domain is maintained at 0.11 m, consistent with the experimental conditions. A spherical particle with a radius of 12.7 mm is released from a decided height above the water surface, replicating the experimental setup. In the experimental study, the spherical particle attained a velocity of 2.17 m/s upon reaching the water's surface. To expedite computational processes and minimize simulation time, we have initially positioned the spherical particle at the water's surface with an initial velocity matching that observed in the experimental investigation, as per the approach adopted in previous numerical studies (Xu et al., 2019). To examine the accuracy of the proposed method, this validation has been done on three scenarios with different densities: (I) 860 (kg/m^3), (II) 1140 (kg/m^3), and (II) 2300 (kg/m^3). The overall domain configuration is depicted in Fig. 5, while Table 1 provides detailed specifications of the numerical parameters employed in this simulation.

The dynamic evolution of the sphere's impact on the water surface for the lightest sphere (i.e., scenario (I)) is visually described in both 3D and 2D representations, as illustrated in Fig. 6 and Fig. 7, respectively. These visualizations clearly depict the fluid-particle interaction dynamics captured by our proposed framework. Particularly, the framework accurately reproduces the smooth interaction surface between the fluid and the particle, while effectively capturing the formation of water splashes resulting from the impact.

The results obtained from the simulation represent the impact between the sphere and the fluid, as showcased in Fig. 6(a) and Fig. 7(a). In these representations, it is clear that the sphere displaces the fluid laterally as it enters the fluid medium. At the same time, the fluid is forced to circumvent the sides of the sphere to accommodate its entry.

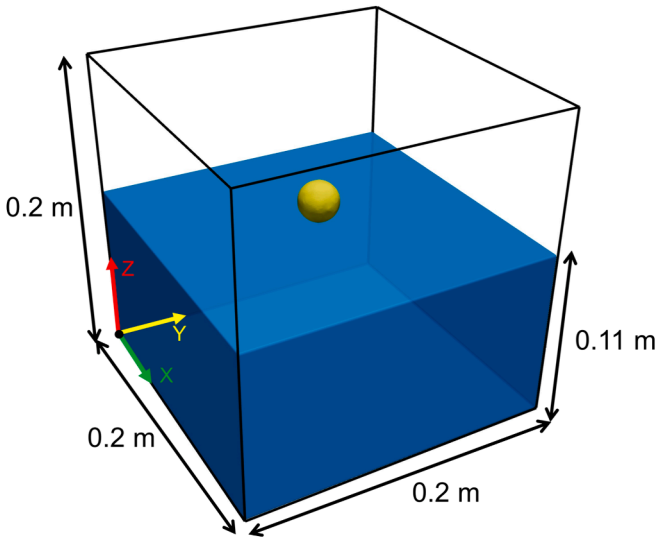

Fig. 5. Initial 3D domain of the sphere water entry validation case.

Therefore, as the sphere progresses deeper into the water, a cavity forms in its wake, as depicted in Fig. 6(b) and Fig. 7(b). As the sphere continues its inclination, the pressure exerted by the surrounding fluid on the cavity's sidewalls increases, causing the cavity to constrict, particularly near the sphere's upper surface, as shown in Fig. 6(c) and Fig. 7(c). Eventually, this pressure buildup results in the detachment of the cavity from the sphere, causing the water to surge upwards. Besides, due to the lower density of the sphere compared to the surrounding fluid, the buoyant force exceeds the gravitational force acting on the sphere, leading to a reduction in its vertical acceleration over time. Furthermore, the simulation demonstrates that the sphere exhibits negligible lateral motion (i.e., in the x and y-directions), highlighting the accuracy

Table 1
Properties of particles used in the sphere water entry validation case.

Property	Value
Time step (s)	1×10^{-5}
Fluid Density (kg/m^3)	1000
Kinematic viscosity coefficient (m^2/s)	1×10^{-6}
fluid particle size (m)	5×10^{-4}
Particle Density (kg/m^3)	860, 1140, 2300
Normal Stiffness (N/m)	3×10^4
Shear Stiffness (N/m)	2.7×10^4
Friction coefficient	0.4
Particle Radius (mm)	12.7

of the proposed method in capturing the fluid-particle interaction dynamics.

The accuracy of the developed framework was assessed by comparing the results obtained from SPH-iDEM with those of previous experimental and theoretical investigations (Aristoff and Bush, 2009). This comparison, illustrated in Fig. 8, indicates a good agreement between the model predictions and the established experimental and theoretical findings for all simulated densities. Furthermore, the impact of damping on the sphere's vertical displacement is clear in the slope of the depth versus time curve. As the sphere descended deeper into the fluid medium, the vertical uplift force exerted by the surrounding fluid, calculated through the coupling, increased owing to the lower density of the sphere relative to the fluid. This comparison, therefore, not only highlights the accuracy of the model but also confirm the efficacy of the proposed SPH-iDEM coupling strategy within the specified simulation setup outlined in Table 1.

3.2. Cube Settlement in Water

In this section, we validate our method by comparing the results obtained from SPH-iDEM with experimental data from a previous study (Wu et al., 2014) on the behavior of a half-submerged cube particle. Our primary objective is to assess the accuracy of the proposed method in capturing the hydrodynamic and gravitational forces acting on a grain with a sharp edge, possessing a higher density than the surrounding water. The initial setup and simulation properties are illustrated in Fig. 9 and summarized in Table 2, respectively. Through this validation, we aim to demonstrate the performance of our approach in replicating the complex interactions between the cube particle and the surrounding fluid, including the hydrodynamic effects induced by its distinctive geometric features and density contrast.

The settling process of the dense cube in the water is visually depicted in Fig. 10. Initially, the gravitational force acting on the cube induces settlement, displacing the water to the sides; see Fig. 10(a). As observed previously with the sphere case, this settling action creates a cavity above the cube. However, due to the cube's zero initial velocity, the depth of the resulting cavity channel is not as significant as in the sphere case. Therefore, as the cube continues to descend into the water, the pressure exerted by the surrounding fluid gradually compresses the cavity channel, eventually causing it to close above the cube. Consistent with expectations, the cube exhibits no rotational or lateral movements throughout the settling process, further confirming the accuracy of our coupling approach.

In order to assess the performance of our SPH-iDEM coupling, we conducted a quantitative comparison between the vertical position (in the Z-direction) of the cube obtained from our simulation and experimental data (Wu et al., 2014). As illustrated in Fig. 11, our numerical framework exhibited an excellent accuracy, as shown by the close alignment between our simulation results and the experimental data.

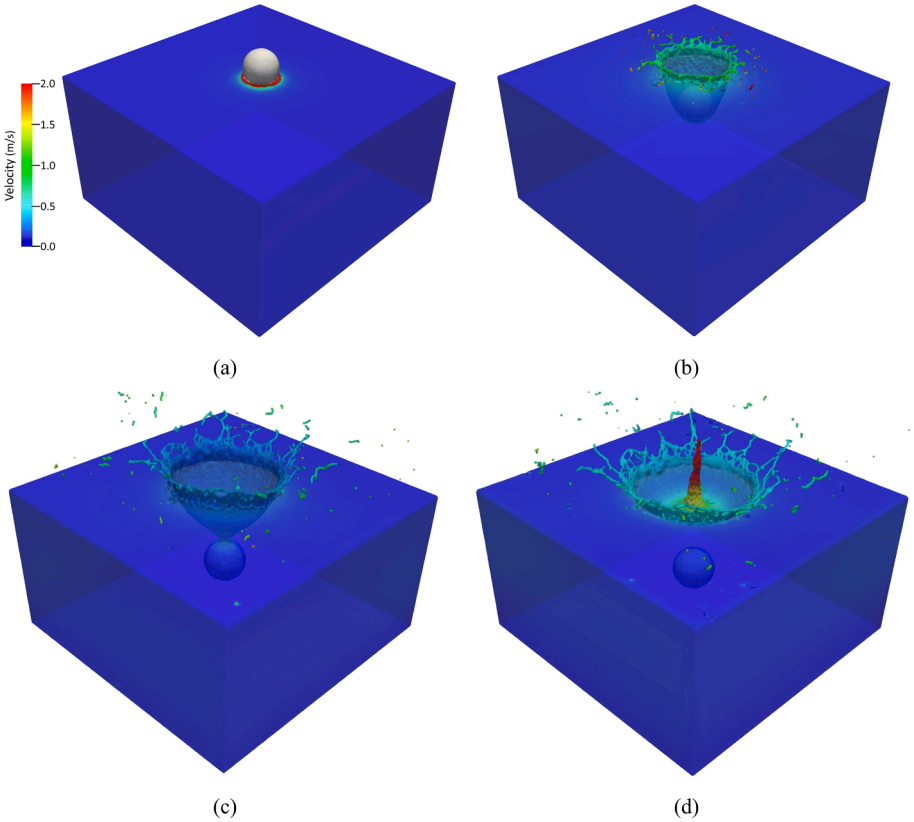

Fig. 6. 3D illustration of the dynamic evolution of the water entry validation case at (a) t = 0.003 s, (b) 0.025 s, (c) 0.075 s, and (d) 0.1 s for the sphere's density 860 (kg/m^3) (i.e., scenario (I)).

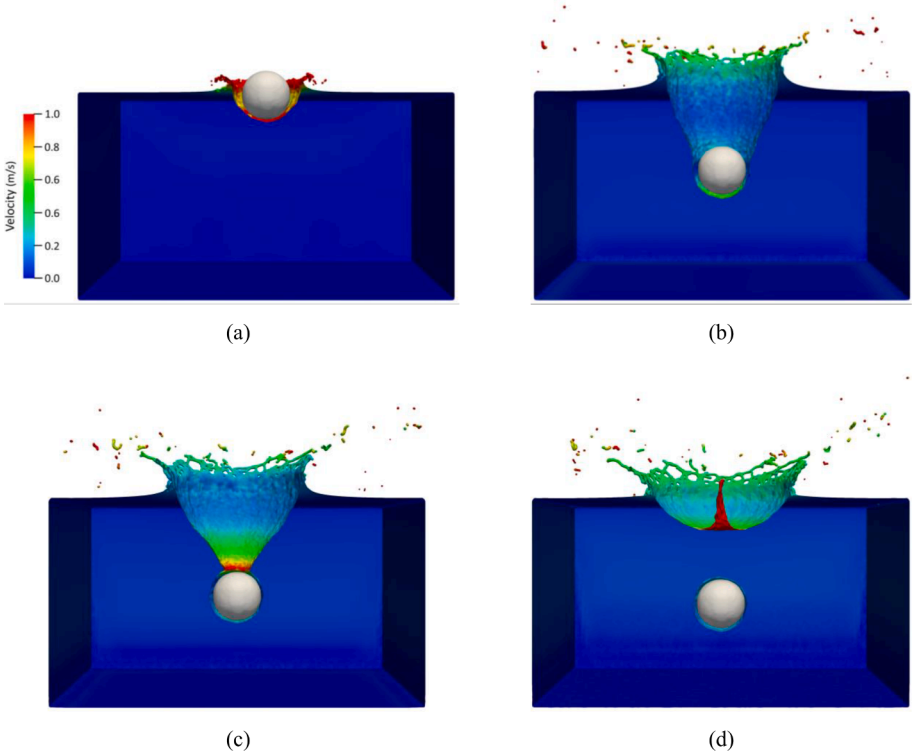

Fig. 7. 2D demonstration of the dynamic evolution of the sphere water entry validation case at (a) t = 0.01 s, (b) 0.05 s, (c) 0.07 s, and (d) 0.09 s for the sphere's density 860 (kg/m^3) (i.e., scenario (I)).

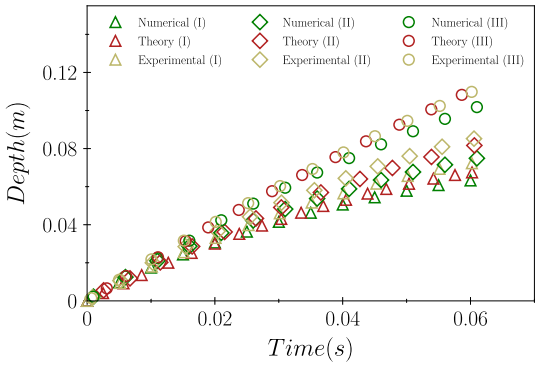

Fig. 8. Time evolution of the sphere Z-direction (i.e., vertical) displacement in the water-entry validation case compared to the experimental results and theoretical solution.

4. Case Study: Dam Break of Irregular and Cube Particles

In this section, we apply our validated SPH-iDEM framework to investigate the dam break problem. The initial configuration of the domain is depicted in Fig. 12. To demonstrate the versatility of our method and the influence of particle shape, we considered two setups: one with cubic particles and another with irregular particles. Both particle types are designed to have identical mass and volume for consistency. The average radius of particles is set to 37.5 mm in both cases. To minimize the effects of initial settling, we allow the particles to settle for a brief period after positioning them at the same location. The produced models can be seen from different angles in Fig. 12(b) and (c). As can be seen, the irregular particles exhibit greater compactness and interlocking after the initial settling phase, attributed to the irregularity in their shape. Conversely, this phenomenon is not observed in the cubic grain setup. Further details regarding the simulation parameters for both

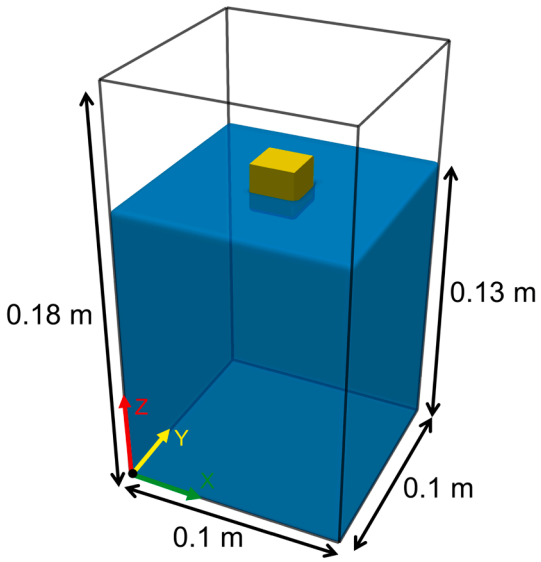

Fig. 9. Initial 3D domain of the cube settlement in water validation case.

cubic and irregular particle configurations are provided in Table 3. Properties of particles used in the cube and irregular dam break simulations..

The dynamic evolution of the dam break process for irregular particles is depicted in Fig. 13. Initially, at the point of impact (Fig. 13(a)), the fluid exhibits its highest velocity. As the fluid interacts with the irregular particle assembly (acting as moving obstacles), it splashes in lateral and vertical directions to accommodate the irregularities (Fig. 13 (b)). At the same time, the irregular particles experience sudden movements induced by the impact of the fluid. As time progresses, the wave generated in the fluid gradually settles, resulting in a decrease in

Table 2
Properties of particles used in the cube settlement validation case.

Property	Value
Time step (s)	1×10^{-5}
Fluid Density (kg/m^3)	996.51
Kinematic viscosity coefficient (m^2/s)	1×10^{-6}
fluid particle size (m)	1×10^{-3}
Particle Density (kg/m^3)	2120
Normal Stiffness (N/m)	3×10^4
Shear Stiffness (N/m)	2.7×10^4
Friction coefficient	0.4
Cube size (mm)	20

wave amplitude (Fig. 13(c)). During these time steps, the side flows experience the highest velocities due to the presence of the irregular particles obstructing the flow and making a channel with the walls. As the fluid reaches the end of the domain, a backward wave is created (Fig. 13(d)). In the following time steps (Fig. 13(e) and (f)), the irregular particles become submerged in the water, and their backward movements are constrained due to the limited fluid force acting upon them. Essentially, although the force from the dam break causes significant movement of the irregular particles, the backward wave propagation is restricted by the presence of the particles and the domain boundary, leading to energy dissipation.

The fluid velocity profile for cube particles is illustrated in Fig. 14. Similar to the irregular case, the highest water velocity occurs at the moment of impact for the cube grain scenario (Fig. 14(a)). Additionally, owing to the initial height of the cubic particle assembly, the water wave generated during impact is more pronounced. Following the impact, the side channel flows exhibit the highest velocities due to the absence of grain resistance in such spaces, similar to the irregular case. Furthermore, a comparison of the time evolution reveals that cube grains undergo greater lateral movement compared to irregular particles, likely due to manifesting a large surface area and a clear void space between such objects. These reason can enhance the movement of the cubes relative to the irregular pack, as evidenced by a comparison of Fig. 13 and Fig. 14. Similar to the irregular grains, energy damping is observed in the cubic grains, with the backward wave unable to propagate as far as the initial dam break wave. Another important observation is the volume of water trapped behind the particle assembly in each case. A comparison of Fig. 13(d) and Fig. 14(d) reveals that the irregular particle assembly retains a larger volume of water compared to the cubic particles.

Based on the observed flow behaviors depicted in Fig. 13 and Fig. 14, the dam break problem exhibits four distinct phases: 1. The initial collapse of the water volume, 2. The impact between the water and moving obstacles, 3. The motion of the grains until the end of the channel, and 4. The interaction of the water with the end of the channel, resulting in the formation of a backward wave. While the first phase remains unaffected by the shape of the grains, the second phase is particularly influenced by grain shape, varying the fundamental behavior of fluid motion both during this phase and thereafter. Furthermore, it was observed that the backward wave has minimal effect on the movement of both types of particles within this setup.

After examining the fluid velocity, analyzing fluid pressure distribution can provide further insights. Fig. 15 illustrates the pressure

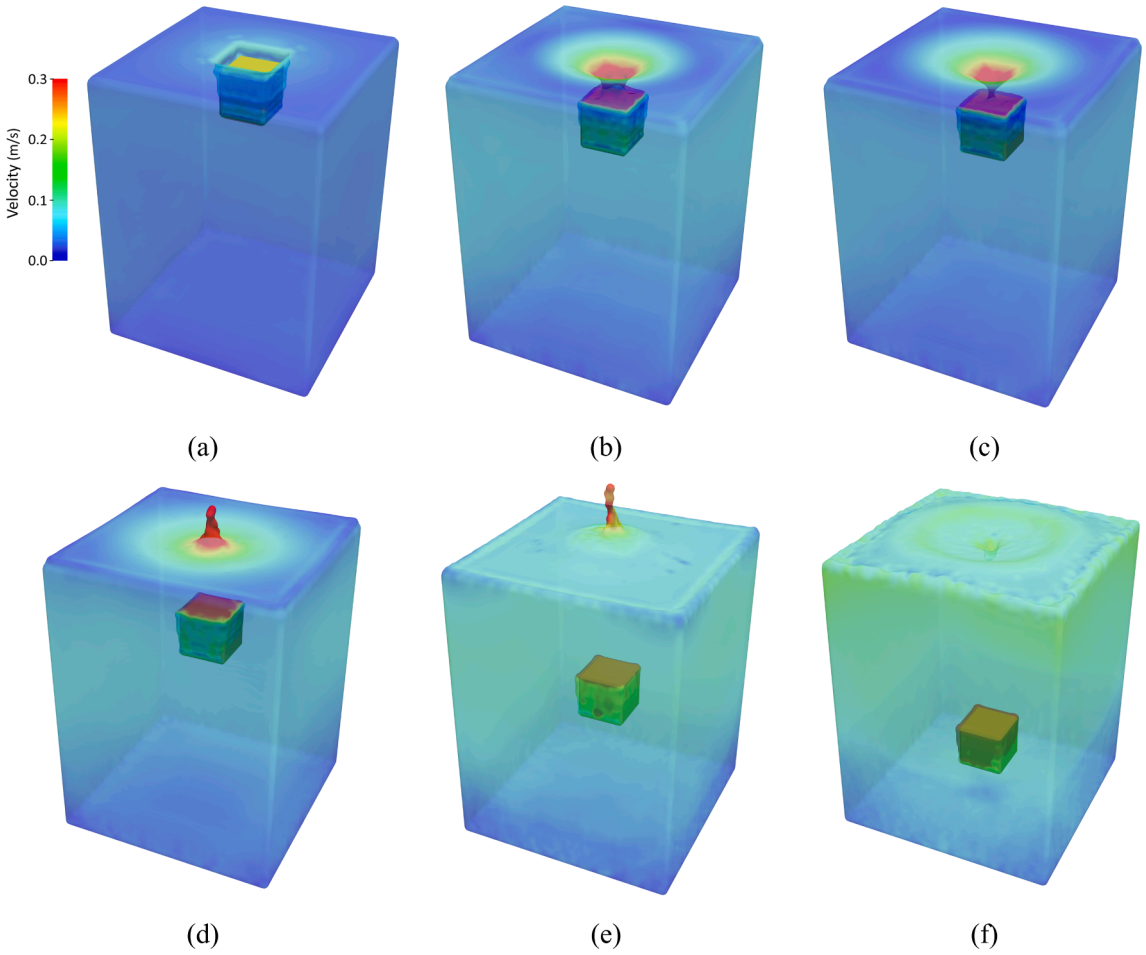

Fig. 10. 3D illustration of the dynamic evolution of the cube settlement in water validation case at (a) t = 0.08 s, (b) 0.12 s, (c) 0.127 s, (d) 0.16 s (e) 0.24 s, and (f) 0.32 s.

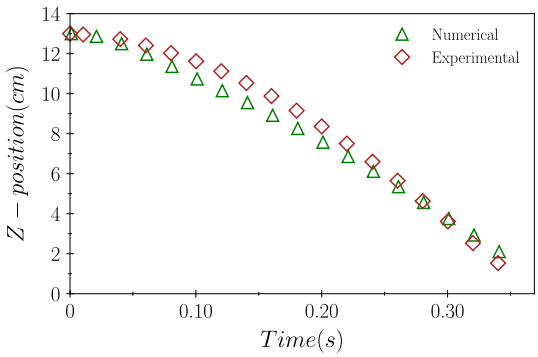

Fig. 11. Comparison between SPH-iDEM results with the previous experimental study with respect to the vertical position of the cube in the settlement validation case during time.

distribution in the fluid throughout the simulations. As depicted in Fig. 15(a), pressure is naturally higher at the bottom of the domain, consistent with hydrostatic pressure principles. However, during the impact phase, the highest-pressure region in the system (as observed in Fig. 15(a)) is situated behind the irregular pack. This elevated pressure can be attributed to the resistance encountered by the grains due to inertia, despite their ability to move. In addition, Fig. 13(a) illustrates the lowest velocity at the impact region, contributing to the higher pressure observed.

Furthermore, high-pressure regions are visibly seen on the grains due to the resistance mentioned earlier. Although the fluid exhibits high pressure behind the irregular particles at the moment of impact (Fig. 15 (a)), this pressure diminishes thereafter in those regions (Fig. 15(b)). This behavior can be attributed to the redistribution of pressure caused by the fluid's redistribution in the domain. At a specific time-step (t = 0.38 s), depicted in Fig. 15(b), the wave exhibits the lowest pressure values, as expected, given its freedom of movement. Even after the dissipation of the wave, high-pressure regions persist just behind the grains (see Fig. 15(d) and (c)), while the lowest pressure is observed in the side channels, where no obstacles impede fluid flow. This observation is consistent with our previous visualization in Fig. 13(c), where the side channels exhibited the highest velocity, facilitating easier fluid movement and thus lower pressure. Our results (Fig. 15(d)) further

Table 3
Properties of particles used in the cube and irregular dam break simulations.

Property	Value
Time step (s)	25×10^{-6}
Fluid Density (kg/m^3)	1000
Kinematic viscosity coefficient (m^2/s)	1×10^{-6}
fluid particle size (m)	5×10^{-3}
Grain's density (kg/m^3)	1250
Normal Stiffness (N/m)	3×10^4
Shear Stiffness (N/m)	2.7×10^4
Friction coefficient	0.4
Grain's average radius (mm)	37.5

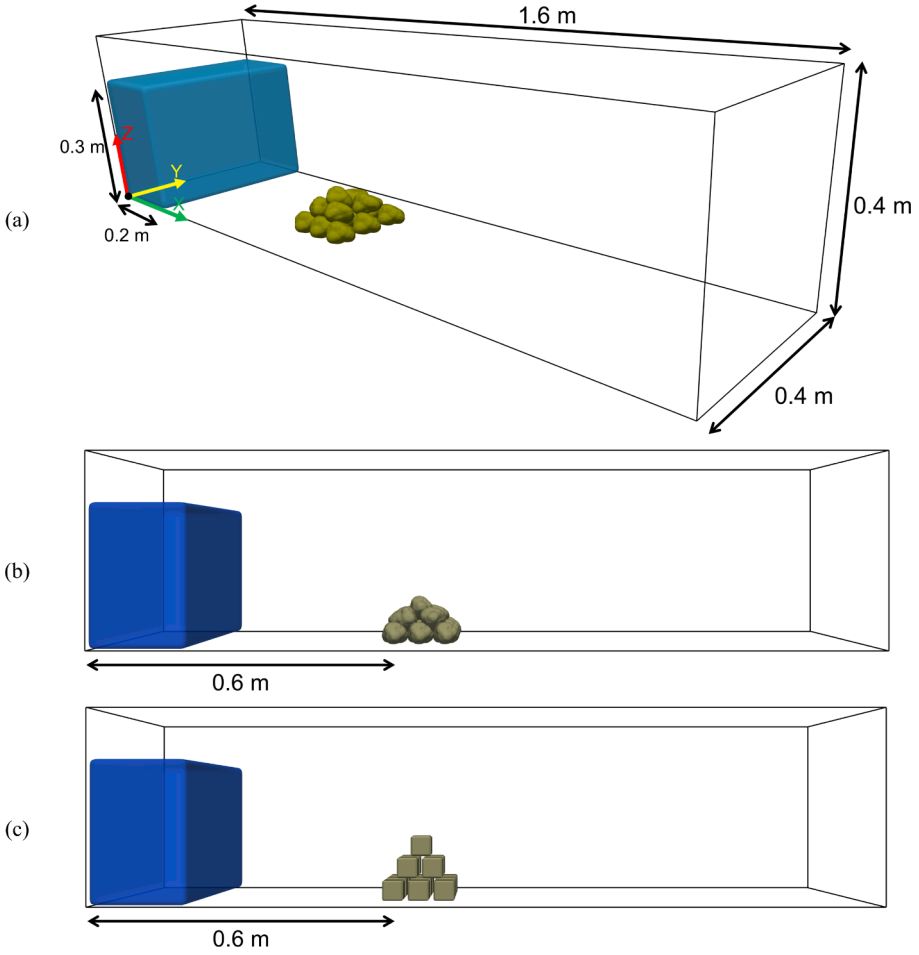

Fig. 12. 3D illustration of (a) the size of the domain and initial position and dimensions of water volume and the position of irregular particles, and side view of the initial arrangement of (b) irregular and (c) cube grains at the start of the SPH-iDEM simulations after grain settlement.

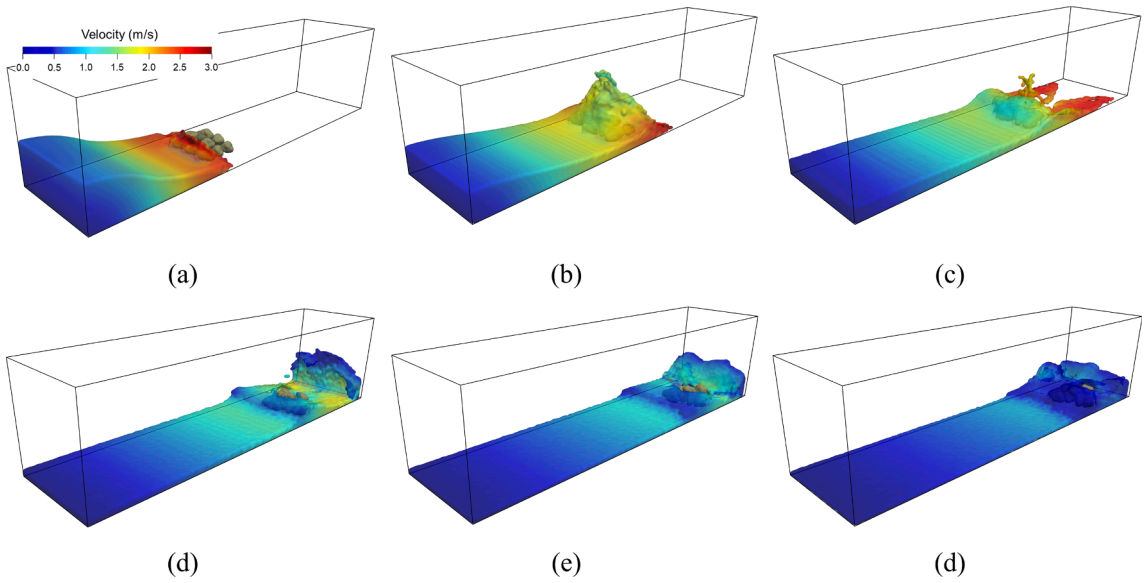

Fig. 13. 3D dynamic evolution of dam break process for irregular grains simulation with respect to the velocity of fluid particles at (a) t = 0.25 s, (b) t = 0.38 s, (c) t = 0.57 s, (d) t = 0.88 s, (e) t = 1.08 s, and (f) t = 1.3 s.

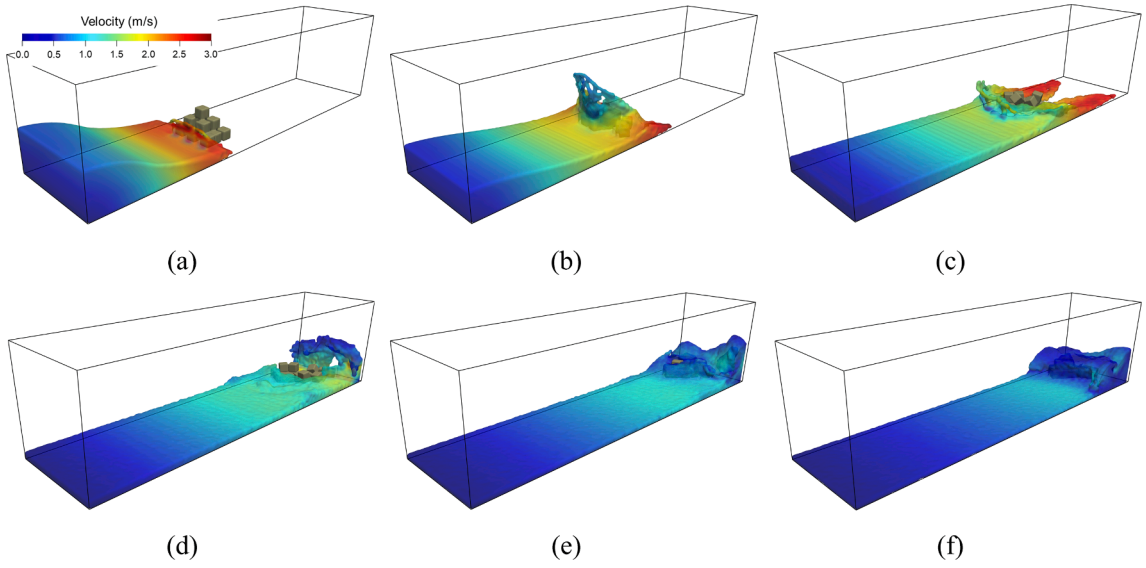

Fig. 14. 3D dynamic evolution of dam break process for cube grains simulation with respect to the velocity of fluid particles at (a) t = 0.25 s, (b) t = 0.38 s, (c) t = 0.57 s, (d) t = 0.88 s, (e) t = 1.08 s, and (f) t = 1.3 s.

indicate an increase in fluid pressure upon impacting the downstream wall. Immediately after the formation of the backward wave (Fig. 15(d) and (e)), pressure rises around the grains due to inertia, as the fluid exerts limited movement on them. Fig. 15(f) illustrates a combination of hydrostatic pressure resulting from the water depth and increased pressure in the grain regions.

It will also be necessary to analyze the pressure distribution in the cubic case due to the interesting phenomena captured in the irregular case. To do so, Fig. 16 demonstrates the pressure distribution. The previously observed highest-pressure areas upstream of the cubic particles can also be seen (Fig. 16(a)). However, the shape of this pressure region differs from that of the irregular case. In the cubic case, the high-pressure area is more spread out compared to the irregular one, highlighting the influence of the shape of grains in such systems.

Furthermore, when comparing Fig. 15(b) and Fig. 16(b), it is clear that the high-pressure zone behind the cube pack is smaller than in the irregular case, indicating that the cube grains offer less resistance to fluid flow while irregular particle show some degree of interlocking. Therefore, fluid can flow through the cubic pack more easily, leading to a more distributed pressure profile in this scenario. This trend is also noticeable in the comparison between Fig. 15(c) and Fig. 16(c). Therefore, a greater volume of water can reach the downstream wall in the cube case compared to the irregular particle setup, as depicted in Fig. 15 (d) and Fig. 16(d). As a result, water pressure is higher in those regions (i.e., downstream wall) in the cube case. Another important difference between irregular and cubic setups is that at the same time (t = 1.08 s), the pressure is higher and more evenly distributed throughout the domain in the cubic case, whereas in the irregular particle scenario, more fluid is trapped behind the irregular pack, as demonstrated in Fig. 15(e) and (f).

Studying the fluid kinetic energy for irregular and cubic packs provides further insights into the system behavior. In Fig. 17, a comparison between the cubic and irregular cases regarding the fluid's kinetic energy is presented. At the moment of impact (Fig. 17(a) and (d)), one can

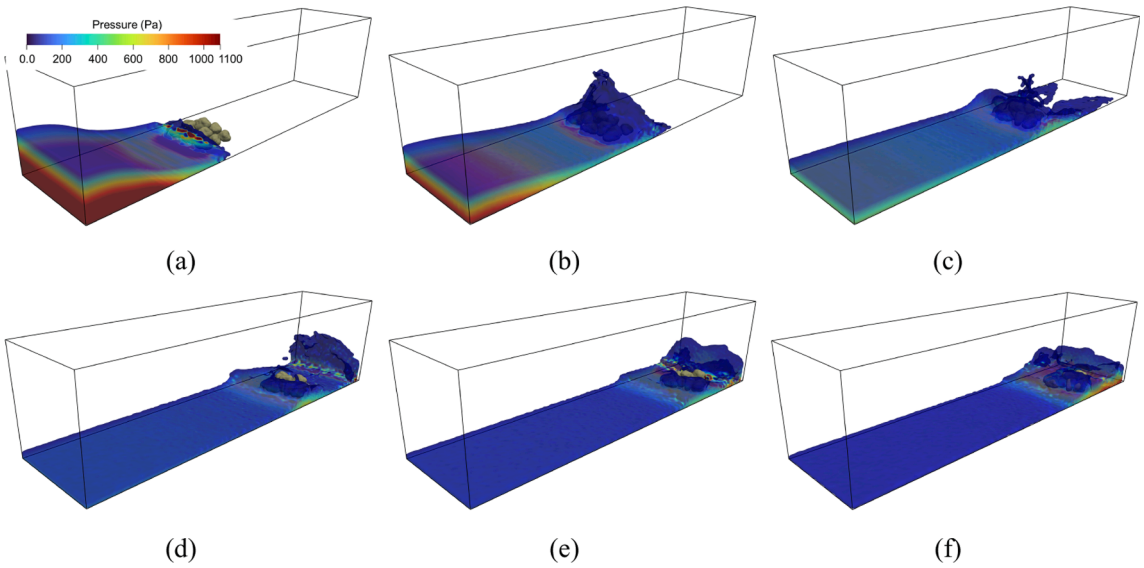

Fig. 15. 3D dynamic evolution of fluid pressure in dam break process for irregular grains simulation at (a) t = 0.25 s, (b) t = 0.38 s, (c) t = 0.57 s, (d) t = 0.88 s, (e) t = 1.08 s, and (f) t = 1.3 s.

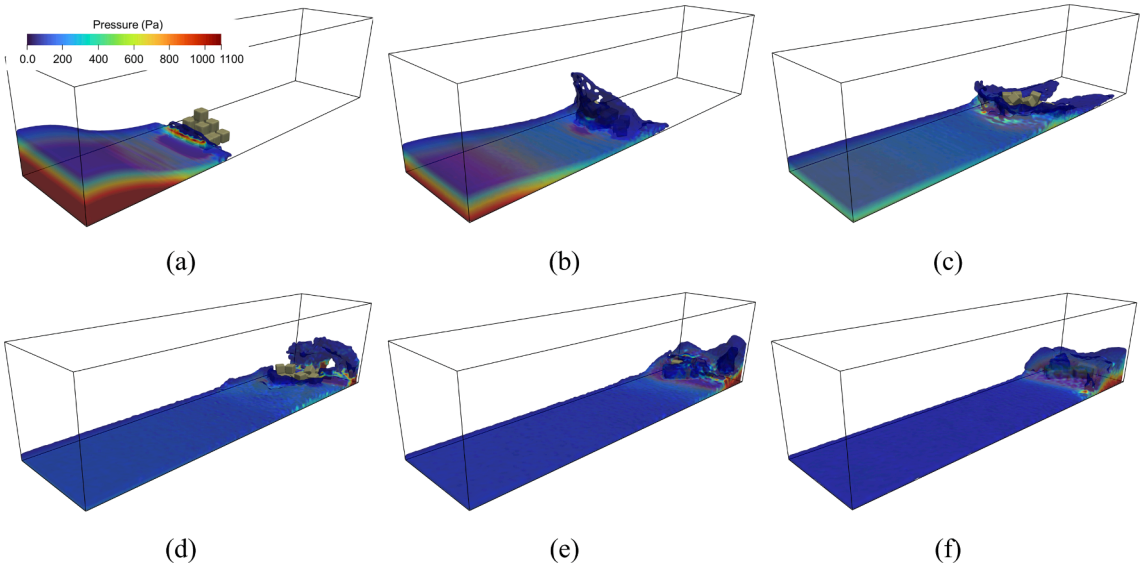

Fig. 16. 3D dynamic evolution of fluid pressure in dam break process for cube grains simulation at (a) t = 0.25 s, (b) t = 0.38 s, (c) t = 0.57 s, (d) t = 0.88 s, (e) t = 1.08 s, and (f) t = 1.3 s.

see that the fluid in the cubic pack possesses higher kinetic energy, consistent with our previous observations of velocity and pressure fields. However, a reverse trend is observed over the packs, where the fluid wave generated after impact (Fig. 17(b) and (e)) exhibits more energy in the irregular case. This reversal can be attributed to the movement of the grains. The fluid can move the cubic particles more readily due to dealing with a large surface area, resulting in less resistance within the cubic pack and thus less energy in the created wave. In contrast, irregular particles form a higher obstruction, causing the fluid wave to attempt to pass over them rather than through, leading to a higher energy wave. Furthermore, towards the end of the simulation, there is no significant difference in kinetic energy between these cases, as by this stage, the initial kinetic energy from the dam break has dissipated into the system (Fig. 17(c) and (f)).

To quantitatively analyze the movement of cubic and irregular particles in the dam break system, we present Fig. 18. In Fig. 18(a), the average X-direction displacement (i.e., the direction of the longest length) of all cubic and irregular particles is illustrated. Initially, there is no change in displacement for either cube or irregular particles, indicating that the particles are fully settled. However, upon the impact of fluid and grains, both types of particles experience significant downstream movement such that cube particles exhibit greater movement than irregular grains, consistent with our previous observations of lateral movement dominance by cube particles. Another important trend in Fig. 18(a) is that cubic grains cease displacing sooner than irregular particles which is attributed to the fluid reaching the end of the domain in the cube case, leading to the formation of the backward wave discussed earlier. The influence of this wave is apparent in a slight decrease in X displacement, indicating backward movement induced by the wave. In addition to X displacement, studying Z displacement yields valuable insights. Fig. 18(b) illustrates the average Z displacement of grains. Clearly, cube particles experience more negative Z displacement, a consequence of their initial formation resulting in a greater height for the cubic pack. Conversely, although irregular particles exhibit a similar

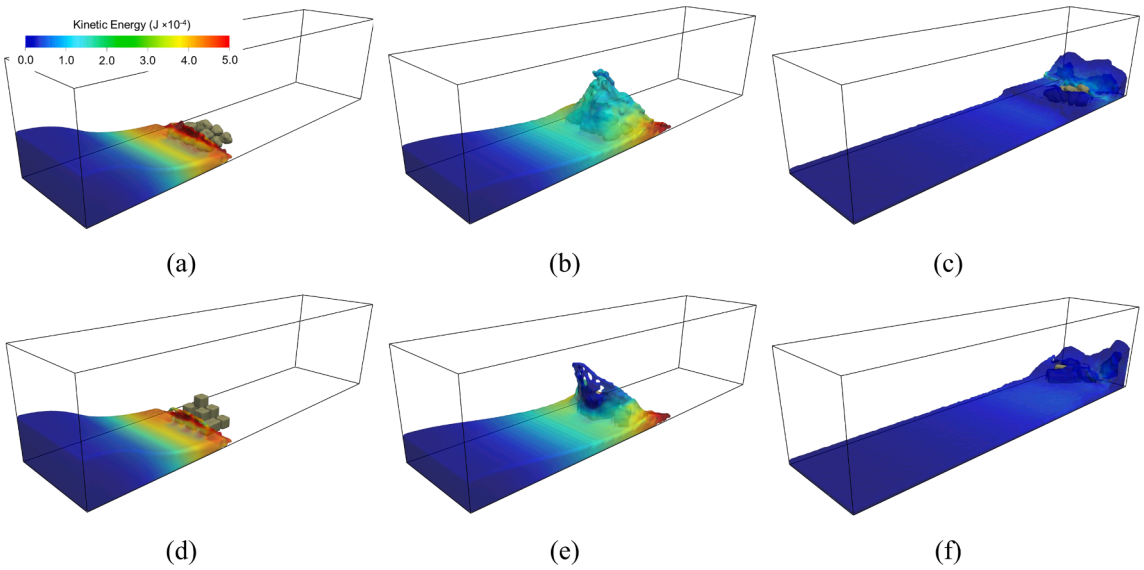

Fig. 17. 3D dynamic evolution of fluid kinetic energy in dam break process for irregular grains simulation at t = 0.25 s for (a) irregular and (d) cube, at t = 0.38 s for (b) irregular and (e) cube, at t = 1.08 s for (c) irregular and (f) cube.

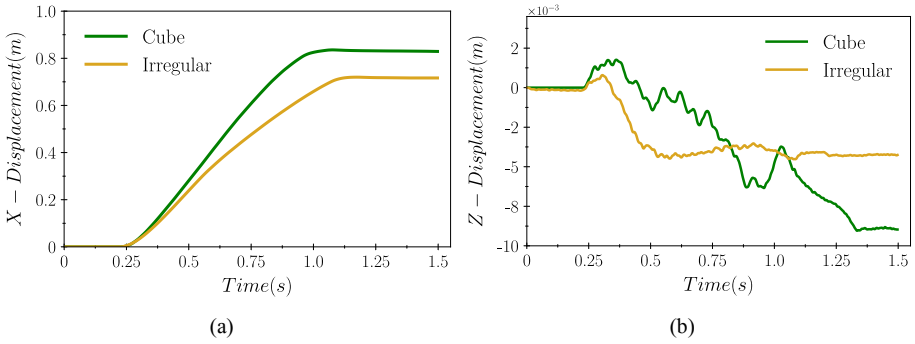

Fig. 18. Time evolution of average (a) X displacement and (b) Z displacement of the cube and the irregular pack.

trend in Z displacement, due to the interlocking and initial formation of them, they experienced a lower Z displacement. However, given that cube particles exhibit greater overall movement, their average Z displacement is higher than that of irregular particles, as expected.

After analyzing the average motions of particles, we now examine the X and Z positions of the top grains in both the cube and irregular packs, as depicted in Fig. 19. Consistent with the average displacement trends shown in Fig. 18(a), the X position of the top grains follows a similar pattern. Similarly, the Z position of the top grains reflects the same trends observed in the average Z displacement. Initially, both types of grains experience an increase in Z location due to the impact, but this increase is more pronounced for the cubic grains due to their higher elevation. Additionally, as observed earlier, fluid flow in the cubic case is faster and more unrestricted compared to the irregular case, leading to more significant changes in the Z direction for the top cube grain. These findings align well with previous numerical investigations (Canelas et al., 2016; Sun et al., 2023).

Up to this point, we have analyzed and compared various aspects of the dam break problem, including fluid velocity, pressure, kinetic energy, average particle displacement, and the positions of top grains in both the X and Z directions. To further enhance our understanding, we examine the average particle velocity, as illustrated in Fig. 20. Fig. 20(a)

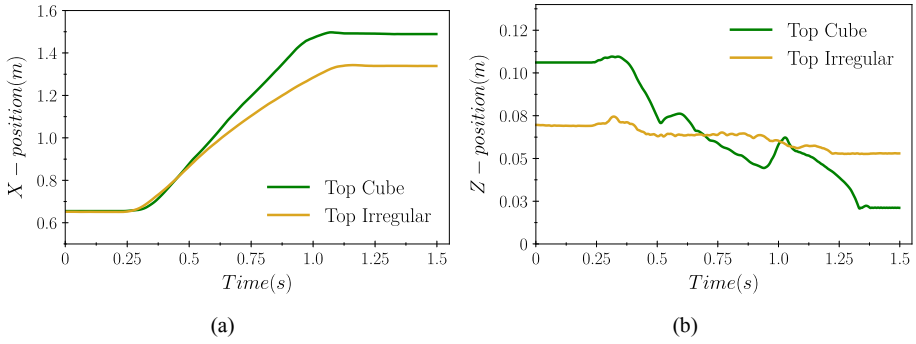

Fig. 19. Time evolution of top particle's (a) X and (b) Z positions in the cube and the irregular pack.

indicates that cube grains generally exhibit higher average velocities throughout most of the simulation period. This observation aligns with our expectations and visual observations, given a larger surface area, which facilitates greater fluid velocity and kinetic energy. For a more quantitative comparison between cube and irregular particles, we plot the velocity difference as a percentage of the velocity of irregular particles, represented by the equation $(= (V_{irregular} - V_{cube})/V_{irregular})$, as shown in Fig. 20(b). Here, positive values indicate instances where irregular particles have higher velocities, while negative values signify higher velocities for cube particles. Although irregular particles occasionally exhibit higher velocities, reaching around 60% higher, cube grains generally maintain higher velocities, surpassing irregular particles by over 80% at certain points during the simulation.

5. Summary and conclusion

The calculation of fluid-particle interaction is crucial in numerous research fields due to its significant impact on natural phenomena. Furthermore, previous investigations have emphasized the significance of particle shape in such systems. In this study, our objective was to develop a numerical framework capable of accurately computing fluid-particle interactions involving complex, irregularly shaped particles. To achieve this, we implemented a coupling between SPH and our previously introduced Image-based Discrete Element Method iDEM. Within the SPH-iDEM coupling framework, the SPH component handles fluid interactions, while the iDEM component models the behavior of irregular particles within the simulation domain.

To demonstrate the effectiveness of our proposed method, we initiated by validating our coupling approach using the sphere water entry problem. This scenario involved a sphere penetrating a quiescent water tank at a defined velocity, replicating conditions from prior experimental investigations. Our SPH-iDEM simulations produced results consistent with both experimental and theoretical solutions, effectively capturing phenomena such as cavity flow behind the sphere and water necking in these regions. We also conducted another validation case involving a cube in a water settlement simulation, based on a prior experimental study. Unlike the sphere water entry case, the cube in this validation test was initially at rest, but with a density higher than that of the fluid. Despite this difference, our developed coupling scheme demonstrated its capability and accuracy in reproducing experimental results for this scenario as well.

Once our numerical coupling scheme was successfully validated, we proceeded to apply it to a more complicated scenario: the classic dam break problem involving moving obstacles (i.e., grains). To account for the influence of particle shape in this problem, we designed two simulations: one with irregular particles and the other with a cube of equal mass and volume. To ensure the grains were stationary, we allowed them to settle completely before initiating the simulation. Then, we released the water volume into the system and observed the fluid's motion, velocity, pressure, and kinetic energy. Our analysis revealed that the dam break problem unfolds in four distinct phases: (*i*) the initial collapse of the water volume, (*ii*) the first impact of the fluid with the grain pack, (*iii*) the distribution of the fluid after impact, and (*iv*) the formation of a backward wave when the water volume collides with the downstream boundary wall. Among these phases, we identified that the second phase (impact with the grain pack) exerted the most significant influence on subsequent steps.

Based on our comprehensive analysis, both irregular and cubic grains exhibited significant movement during the water impact phase, with the cubic grains demonstrating higher displacement due to the shape of such objects and having a large surface area. Aside from this, a comparison of fluid velocity distributions revealed the formation of two prominent flow channels alongside the grain packs, where fluid velocity was particularly higher due to reduced grain resistance. Furthermore, our investigation into fluid pressure distribution showed that pressure peaked behind the grains upon impact, while it remained lowest in the side channel flows. The cubic pack scenario demonstrated higher fluid kinetic energy, attributed to its greater void spaces facilitating smoother fluid flow. Conversely, the irregular grain pack exhibited higher resistance, resulting in greater dampening of fluid kinetic energy. Moreover, our analysis of particle displacement and top particle positions supported earlier quantitative findings, with cubic particles indicating greater motion. Finally, examination of average grain velocity illustrated that cubic particles experienced around 80 % higher velocity, underlining the significance of grain shape in influencing fluid-particle interactions in such scenarios.

The proposed SPH-iDEM method demonstrated its efficiency and accuracy in modeling fluid-particle interactions by accurately capturing the natural shape of grains. This capability opens avenues for applying SPH-iDEM to address fluid and irregular particle dynamics in various complex and large systems when using the existing mesh-based CFD methos might not be feasible. Although it is not the focus of this study and despite the effectiveness of SPH-iDEM in large scale, the particle-based nature of SPH limits one to capture microscale and nanoscale with desired accuracy systems. Future research directions could involve extending the presented technique to handle scenarios involving multiphase fluid systems in angular particles, thereby expanding the applicability and versatility of the proposed SPH-iDEM approach.

CRediT authorship contribution statement

Mehryar Amir Hosseini: Methodology, Visualization, Validation, Software, Investigation, Data curation. **Pejman Tahmasebi:** Validation, Supervision, Project administration, Methodology, Funding acquisition, Conceptualization.

Declaration of competing interest

The authors declare that they have no known competing financial interests or personal relationships that could have appeared to influence the work reported in this paper.

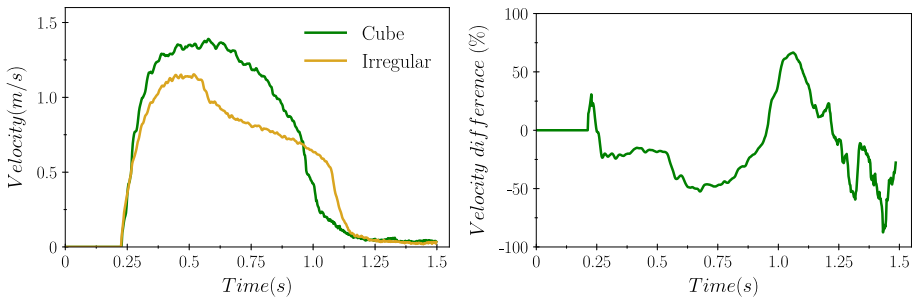

Fig. 20. Time evolution of grains (a) average velocity in the cube and the irregular pack and (b) the velocity difference between cube and irregular packs.

Data availability

Data will be made available on request.

Acknowledgments

We would like to thank the financial support from the Colorado School of Mines for this research. This study was supported by NSF (Grant # CMMI-2000966).

References

Amir Hosseini, M., Kamrava, S., Sahimi, M., Tahmasebi, P., 2023. Effect of Wettability on Two-Phase Flow Through Granular Porous Media: Fluid Rupture and Mechanics of the Media. Chem. Eng. Sci. 269, 118446 https://doi.org/10.1016/J.CES.2023.118446.

Amir Hosseini, M., Tahmasebi, P., 2023. On the influence of the natural shape of particles in multiphase fluid systems: Granular collapses. Comput. Geotech. 162, 105654 https://doi.org/10.1016/j.compgeo.2023.105654.

Amir Hosseini, M., Tahmasebi, P., 2024. Particle deposition and clogging as an Obstacle and Opportunity for sustainable energy. J. Clean. Prod. 446, 141312 https://doi.org/10.1016/J.JCLEPRO.2024.141312.

Ancey, C., Andreini, N., Epely-Chauvin, G., 2013. The dam-break problem for concentrated suspensions of neutrally buoyant particles. J. Fluid Mech. 724, 95–122. https://doi.org/10.1017/JFM.2013.154.

Angelidakis, V., Nadimi, S., Otsubo, M., Utili, S., 2021. CLUMP: A Code Library to generate Universal Multi-sphere Particles. SoftwareX 15. https://doi.org/10.1016/J.SOFTX.2021.100735.

Aristoff, J.M., Bush, J.W.M., 2009. Water entry of small hydrophobic spheres. J. Fluid Mech. 619, 45–78. https://doi.org/10.1017/S0022112008004382.

Asai, M., Li, Y., Chandra, B., Takase, S., 2021. Fluid–rigid-body interaction simulations and validations using a coupled stabilized ISPH–DEM incorporated with the energy-tracking impulse method for multiple-body contacts. Comput. Methods Appl. Mech. Eng. 377, 113681 https://doi.org/10.1016/J.CMA.2021.113681.

Ataie-Ashtiani, B., Shobeyri, G., 2008. Numerical simulation of landslide impulsive waves by incompressible smoothed particle hydrodynamics. Int. J. Numer. Methods Fluids 56, 209–232. https://doi.org/10.1002/FLD.1526.

Azéma, E., Radjai, F., Dubois, F., 2013. Packings of irregular polyhedral particles: Strength, structure, and effects of angularity. Phys. Rev. E 87, 062203. https://doi.org/10.1103/PhysRevE.87.062203.

Bu, S., Li, D., Chen, S., Xiao, C., Li, Y., 2022. Numerical simulation of landslide-generated waves using a SPH-DEM coupling model. Ocean Eng. 258, 111826 https://doi.org/10.1016/J.OCEANENG.2022.111826.

Bui, H.H., Nguyen, G.D., 2021. Smoothed particle hydrodynamics (SPH) and its applications in geomechanics: From solid fracture to granular behaviour and multiphase flows in porous media. Comput. Geotech. 138, 104315 https://doi.org/10.1016/J.COMPGEO.2021.104315.

Canelas, R.B., Crespo, A.J.C., Domínguez, J.M., Ferreira, R.M.L., Gómez-Gesteira, M., 2016. SPH–DCDEM model for arbitrary geometries in free surface solid–fluid flows. Comput. Phys. Commun. 202, 131–140. https://doi.org/10.1016/J.CPC.2016.01.006.

Canelas, R.B., Domínguez, J.M., Crespo, A.J.C., Gómez-Gesteira, M., Ferreira, R.M.L., 2017. Resolved Simulation of a Granular-Fluid Flow with a Coupled SPH-DCDEM Model. J. Hydraul. Eng. 143, 06017012. https://doi.org/10.1061/(asce)hy.1943-7900.0001331.

Capasso, S., Tagliafierro, B., Martínez-Estévez, I., Domínguez, J.M., Crespo, A.J.C., Viccione, G., 2022. A DEM approach for simulating flexible beam elements with the Project Chrono core module in DualSPHysics. Comput. Part. Mech. 9, 969–985. https://doi.org/10.1007/S40571-021-00451-9/METRICS.

Crespo, A.J.C., Gómez-Gesteira, M., Dalrymple, R.A., 2007. Boundary Conditions Generated by Dynamic Particles in SPH Methods. Comput. Mater. Contin. 5, 173–184. https://doi.org/10.3970/CMC.2007.005.173.

Cundall, P.A., Strack, O.D.L.L., 1979. A discrete numerical model for granular assemblies. Géotechnique 29, 47–65. https://doi.org/10.1680/geot.1979.29.1.47.

Domínguez, J.M., Fourtakas, G., Altomare, C., Canelas, R.B., Tafuni, A., García-Feal, O., Martínez-Estévez, I., Mokos, A., Vacondio, R., Crespo, A.J.C., Rogers, B.D., Stansby, P.K., Gómez-Gesteira, M., 2021. DualSPHysics: from fluid dynamics to multiphysics problems. Comput. Part. Mech. 2021 95 9, 867–895. DOI: 10.1007/S40571-021-00404-2.

English, A., Domínguez, J.M., Vacondio, R., Crespo, A.J.C., Stansby, P.K., Lind, S.J., Chiapponi, L., Gómez-Gesteira, M., 2022. Modified dynamic boundary conditions (mDBC) for general-purpose smoothed particle hydrodynamics (SPH): application to tank sloshing, dam break and fish pass problems. Comput. Part. Mech. 9, 1–15. https://doi.org/10.1007/S40571-021-00403-3/TABLES/4.

Farivar, F., Zhang, H., Tian, Z.F., Gupte, A., 2020. CFD-DEM simulation of fluidization of multisphere- modelled cylindrical particles. Powder Technol. 360, 1017–1027. https://doi.org/10.1016/J.POWTEC.2019.11.016.

Fourtakas, G., Dominguez, J.M., Vacondio, R., Rogers, B.D., 2019. Local uniform stencil (LUST) boundary condition for arbitrary 3-D boundaries in parallel smoothed particle hydrodynamics (SPH) models. Comput. Fluids 190, 346–361. https://doi.org/10.1016/J.COMPFLUID.2019.06.009.

He, Y., Bayly, A.E., Hassanpour, A., Muller, F., Wu, K., Yang, D., 2018. A GPU-based coupled SPH-DEM method for particle-fluid flow with free surfaces. Powder Technol. 338, 548–562. https://doi.org/10.1016/j.powtec.2018.07.043.

Höhner, D., Wirtz, S., Kruggel-Emden, H., Scherer, V., 2011. Comparison of the multi-sphere and polyhedral approach to simulate non-spherical particles within the discrete element method: Influence on temporal force evolution for multiple contacts. Powder Technol. 208, 643–656. https://doi.org/10.1016/J.POWTEC.2011.01.003.

Hosseini, M.A., Tahmasebi, P., 2024. A novel graph-based 3D breakage method for angular particles with an image-based DEM. Int. J. Rock Mech. Min. Sci. 174, 105640 https://doi.org/10.1016/J.IJRMMS.2024.105640.

Houlsby, G.T.T., 2009. Potential particles: a method for modelling non-circular particles in DEM. Comput. Geotech. 36, 953–959. https://doi.org/10.1016/j.compgeo.2009.03.001.

Kawamoto, R., Andò, E., Viggiani, G., Andrade, J.E., 2016. Level set discrete element method for three-dimensional computations with triaxial case study. J. Mech. Phys. Solids 91, 1–13. https://doi.org/10.1016/j.jmps.2016.02.021.

Kawamoto, R., Andò, E., Viggiani, G., Andrade, J.E., 2018. All you need is shape: Predicting shear banding in sand with LS-DEM. J. Mech. Phys. Solids 111, 375–392. https://doi.org/10.1016/J.JMPS.2017.10.003.

Knight, C., O'Sullivan, C., van Wachem, B., Dini, D., 2020. Computing drag and interactions between fluid and polydisperse particles in saturated granular materials. Comput. Geotech. 117, 103210 https://doi.org/10.1016/J.COMPGEO.2019.103210.

Kong, Y., Li, X., Zhao, J., Guan, M., 2022. Load deflection of flexible ring net barrier in resisting debris flows. Geotechnique. https://doi.org/10.1680/JGEOT.22.00135/ASSET/IMAGES/SMALL/JGEOT.22.00135-F7.GIF.

Lai, Z., Zhao, J., Zhao, S., Huang, L., 2023. Signed distance field enhanced fully resolved CFD-DEM for simulation of granular flows involving multiphase fluids and irregularly shaped particles. Comput. Methods Appl. Mech. Eng. 414, 116195 https://doi.org/10.1016/J.CMA.2023.116195.

Li, C.Q., Xu, W.J., Meng, Q.S., 2015. Multi-sphere approximation of real particles for DEM simulation based on a modified greedy heuristic algorithm. Powder Technol. 286, 478–487. https://doi.org/10.1016/J.POWTEC.2015.08.026.

Lian, Y., Bui, H.H., Nguyen, G.D., Tran, H.T., Haque, A., 2021. A general SPH framework for transient seepage flows through unsaturated porous media considering anisotropic diffusion. Comput. Methods Appl. Mech. Eng. 387, 114169 https://doi.org/10.1016/J.CMA.2021.114169.

Liu, Z., Ma, H., Zhao, Y., 2021. Comparative study of discrete element modeling of tablets using multi-spheres, multi-super-ellipsoids, and polyhedrons. Powder Technol. 390, 34–49. https://doi.org/10.1016/J.POWTEC.2021.05.065.

Liu, L., Wu, J., Ji, S., 2022. DEM–SPH coupling method for the interaction between irregularly shaped granular materials and fluids. Powder Technol. 400, 117249 https://doi.org/10.1016/J.POWTEC.2022.117249.

Ma, G., Bui, H.H., Lian, Y., Tran, K.M., Nguyen, G.D., 2022. A five-phase approach, SPH framework and applications for predictions of seepage-induced internal erosion and failure in unsaturated/saturated porous media. Comput. Methods Appl. Mech. Eng. 401, 115614 https://doi.org/10.1016/J.CMA.2022.115614.

Meng, X., Wang, Y., 2016. Modelling and numerical simulation of two-phase debris flows. Acta Geotech. 11, 1027–1045. https://doi.org/10.1007/S11440-015-0418-4/FIGURES/12.

Pastor, M., Tayyebi, S.M., Hernandez, A., Gao, L., Stickle, M.M., Lin, C., 2023. A new two-layer two-phase depth-integrated SPH model implementing dewatering: Application to debris flows. Comput. Geotech. 153, 105099 https://doi.org/10.1016/J.COMPGEO.2022.105099.

Pozzetti, G., Peters, B., 2018. A multiscale DEM-VOF method for the simulation of three-phase flows. Int. J. Multiph. Flow 99, 186–204.

Saucedo-Zendejo, F.R., Reséndiz-Flores, E.O., 2023. Meshfree numerical approach based on the finite pointset method for two-way coupled transient linear thermoelasticity. Comput. Part. Mech. 10, 289–302. https://doi.org/10.1007/S40571-022-00496-4/METRICS.

Shakibaeinia, A., Jin, Y.C., 2011. A mesh-free particle model for simulation of mobile-bed dam break. Adv. Water Resour. 34, 794–807. https://doi.org/10.1016/J.ADVWATRES.2011.04.011.

Sun, J.Z., Zou, L., Govender, N., Martínez-Estévez, I., Crespo, A.J.C., Sun, Z., Domínguez, J.M., 2023. A resolved SPH-DEM coupling method for analysing the interaction of polyhedral granular materials with fluid. Ocean Eng. 287, 115938 https://doi.org/10.1016/J.OCEANENG.2023.115938.

Tahmasebi, P., 2018. Packing of discrete and irregular particles. Comput. Geotech. 100, 52–61. https://doi.org/10.1016/j.compgeo.2018.03.011.

Tahmasebi, P., 2023. A state-of-the-art review of experimental and computational studies of granular materials: Properties, advances, challenges, and future directions. Prog. Mater. Sci. 138, 101157 https://doi.org/10.1016/J.PMATSCI.2023.101157.

Tahmasebi, P., Kamrava, S., 2019. A pore-scale mathematical modeling of fluid-particle interactions: Thermo-hydro-mechanical coupling. Int. J. Greenh. Gas Control. 83, 245–255. https://doi.org/10.1016/j.ijggc.2018.12.014.

Tran-Duc, T., Phan-Thien, N., Khoo, B.C., 2017. A smoothed particle hydrodynamics (SPH) study of sediment dispersion on the seafloor. Phys. Fluids 29, 83302. https://doi.org/10.1063/1.4993474/982481.

Wang, W., Chen, G., Han, Z., Zhou, S., Zhang, H., Jing, P., 2016. 3D numerical simulation of debris-flow motion using SPH method incorporating non-Newtonian fluid behavior. Nat. Hazards 81, 1981–1998. https://doi.org/10.1007/S11069-016-2171-X/TABLES/3.

Wendland, H., 1995. Piecewise polynomial, positive definite and compactly supported radial functions of minimal degree. Adv. Comput. Math. 4, 389–396. https://doi.org/10.1007/BF02123482/METRICS.

Wensrich, C.M., Katterfeld, A., 2012. Rolling friction as a technique for modelling particle shape in DEM. Powder Technol. 217, 409–417. https://doi.org/10.1016/J.POWTEC.2011.10.057.

Wu, T.R., Chu, C.R., Huang, C.J., Wang, C.Y., Chien, S.Y., Chen, M.Z., 2014. A two-way coupled simulation of moving solids in free-surface flows. Comput. Fluids 100, 347–355. https://doi.org/10.1016/J.COMPFLUID.2014.05.010.

Wu, K., Yang, D., Wright, N., 2016. A coupled SPH-DEM model for fluid-structure interaction problems with free-surface flow and structural failure. Comput. Struct. 177, 141–161. https://doi.org/10.1016/J.COMPSTRUC.2016.08.012.

Xiao, Y., Yang, L.M., Du, Y.J., Song, Y.X., Shu, C., 2023. Radial basis function-differential quadrature-based physics-informed neural network for steady incompressible flows. Phys. Fluids 35, 73607. https://doi.org/10.1063/5.0159224/2902185.

Xu, W.J., Dong, X.Y., 2021. Simulation and verification of landslide tsunamis using a 3D SPH-DEM coupling method. Comput. Geotech. 129, 103803 https://doi.org/10.1016/j.compgeo.2020.103803.

Xu, W.J., Dong, X.Y., Ding, W.T., 2019. Analysis of fluid-particle interaction in granular materials using coupled SPH-DEM method. Powder Technol. 353, 459–472.

Xu, T., Huai, W., Liu, H., 2023. MPS-based simulation of dam-break wave propagation over wet beds with a sediment layer. Ocean Eng. 281, 115035 https://doi.org/10.1016/J.OCEANENG.2023.115035.

Zhang, X., Tahmasebi, P., 2018. Micromechanical evaluation of rock and fluid interactions. Int. J. Greenh. Gas Control 76, 266–277. https://doi.org/10.1016/J.IJGGC.2018.07.018.

Zhang, X., Tahmasebi, P., 2019. Effects of Grain Size on Deformation in Porous Media. Transp. Porous Media 129, 321–341. https://doi.org/10.1007/s11242-019-01291-1.

Zhang, X., Tahmasebi, P., 2022a. Investigation of particle shape and ambient fluid on sandpiles using a coupled micro-geomechanical model. Powder Technol. 117711 https://doi.org/10.1016/j.powtec.2022.117711.

Zhang, X., Tahmasebi, P., 2022b. Coupling irregular particles and fluid: Complex dynamics of granular flows. Comput. Geotech. 143, 104624 https://doi.org/10.1016/j.compgeo.2021.104624.

Zhang, X., Tahmasebi, P., 2023. Drafting, Kissing and Tumbling Process of Two Particles: The Effect of Morphology. Int. J. Multiph. Flow 160, 104379. https://doi.org/10.1016/J.IJMULTIPHASEFLOW.2023.104379.

Zhao, J., Zhao, S., Luding, S., 2023. The role of particle shape in computational modelling of granular matter. Nat. Rev. Phys. 2023 59 5, 505–525. DOI: 10.1038/s42254-023-00617-9.

Zhou, Y., Zhou, B., Li, J., Wang, H., 2017. Study on the multi-sphere method modeling the 3D particle morphology in DEM. Springer Proc. Phys. 188, 601–608. https://doi.org/10.1007/978-981-10-1926-5_62/FIGURES/4.